DISPERSION AND ASYMMETRY OF CHIRAL GRAVITATIONAL WAVES IN GYROSCOPIC MECHANICAL SYSTEMS. PART 2: CONTINUUM ASYMPTOTIC MODELS IN EQUATORIAL AND POLAR REGIONS

by A. KANDIAH, I. S. JONES, N. V. MOVCHAN and A. B. MOVCHAN[†]

(Department of Mathematical Sciences, University of Liverpool, Liverpool, L69 7ZL)

[Received October 17, 2024. Revised March 28, 2025. Accepted April 6, 2025]

Summary

The effect of the Coriolis force is demonstrated for chiral continuum models describing waves in the equatorial region and the polar regions on a rotating sphere. Novel asymptotic features of equatorial waves are presented in this paper. We show that the shape of a ridge of a polar vortex can be approximated by the governing equations of a gyropendulum. Theoretical deductions are accompanied by illustrative examples.

1. Introduction

This paper is the second of a series describing the asymptotic approximations and dynamics of chiral gravitational waves in discrete structures and atmospheric and oceanic waves. Equatorial wave phenomena are influenced by the planetary rotation and form an integral part of various aspects of climate processes and oceanography (**1** to **5**). In recent years, advancements in computational techniques and modelling capabilities have enabled researchers to develop increasingly sophisticated continuum models of equatorial waves [see, for example (**6** to **10**)]. These models incorporate parametrisations and simulations, allowing for more accurate predictions of equatorial wave dynamics.

The discrete lattice models in part 1 discussed the chiral features of waves in the elastic three-layer lattice, subjected to gravity and gyroscopic forces, which change their orientation across the central line of the lattice. In those settings, the nodal inertial junctions along the central line are characterised by zero gyricity. Discrete models with gyroscopic components have been analysed in (**11** to **15**). The results of part 1 also include a class of waves that resemble the dispersion of waves known in the literature as the *equatorial inertia-gravity waves* [see (**16**, **17**)]. Although there are similarities between the discrete and continuous settings, we also highlight the differences, particularly in the low-frequency regime. In the present paper, we develop an asymptotic model, that is consistent with the Hadley-cell structure (**18**, **19**) for equatorial waves, in contrast with the analysis presented in

[†]Corresponding author <abm@liverpool.ac.uk>

Q. Jl Mech. Appl. Math, Vol. 78. No. 2 © The Author, 2025. Published by Oxford University Press.

https://doi.org/10.1093/qjmam/hbaf005

(**16**, **17**, **20**, **21**) which includes the study of fields at infinity in the infinite plane. The importance of boundary effects for the Hadley cell is known: in particular, the global circulation pattern of the Hadley cells significantly influences the formation of the world's deserts [see, for example (**22**)]. In addition to the case when the latitude is small (near the equator), we also derive the asymptotic approximation for vortex waves in the polar regions, where the latitude is close to 90°N or 90°S [also, see (**11**, **23**)].

In our analysis, we consider the linearised shallow water equations, in its simplest form, given as follows [see, for example (**17**, **24** to **26**)]:

$$\frac{\partial u}{\partial t} - 2\Omega \sin(\phi) v = -g\frac{\partial h}{\partial x}, \tag{1.1}$$

$$\frac{\partial v}{\partial t} + 2\Omega \sin(\phi) u = -g\frac{\partial h}{\partial y}, \tag{1.2}$$

$$\frac{\partial h}{\partial t} + H\left(\frac{\partial u}{\partial x} + \frac{\partial v}{\partial y}\right) = 0, \tag{1.3}$$

where u and v denote the velocities in the x- and y-directions (or zonal and meridional velocities) respectively, h is the height deviation of the fluid surface, t measures time, H is the depth of the undisturbed fluid, Ω is the angular speed of the rotating body, ϕ is the latitude and g is the gravity acceleration. The terms including the coefficient Ω represent the components of the Coriolis force. The zonal and meridional velocity and height field variables are functions of the horizontal fluid position (x, y) and time t only. The system (1.1)–(1.3) provides an approximate description of a shallow layer of fluid of constant density in the presence of rotation. In our study, we consider a geostrophic approximation, neglect viscous forces, and assume that the surface height deviation is small compared to the depth, that is $h \ll H$.

Equatorial wave dynamics have been extensively explored using models based on the shallow water equations [see, for example (**8**, **17**)]. The study of low-frequency oscillations confined near the equatorial region has been presented in (**27**, **28**). The papers (**16**, **17**, **29**, **30**) considered zonally propagating waves that are exponentially localised near the equator, based on the analysis of the parabolic cylinder functions in an infinite domain. The topological properties of electromagnetic chiral models in connection with equatorial waves are discussed in (**31**, **32**). In the present paper, we construct analytical asymptotic solutions of a model in a narrow equatorial band and use appropriate boundedness conditions at the boundaries of the band in the meridional direction. The analysis is followed by illustrative examples of the types of waves present in such bands: Kelvin waves, inertia-gravity waves and Rossby waves. We show that an equatorial fluid layer, subjected to a variable Coriolis force, can act as a chiral waveguide for propagating inertia-gravity waves and equatorial Rossby waves.

The structure of the paper is as follows. In Section 2, we present a mathematical procedure to obtain asymptotic analytical solutions to the shallow water equations in a narrow band, and discuss the resulting wave motions in connection with the equatorial waves. The refined meridional velocity equation and the new boundary conditions have been derived using the second-order asymptotic procedure, and are fully consistent with the assumptions used in the formulation of the governing (1.1)–(1.3). The equatorial wave dispersion diagrams and examples of eigenfunctions in the vicinity of the equator are provided. We also discuss the analogies between equatorial waves in a continuum and elastic waves in the discrete lattice strip. In Section 3, a formal description of the gyropendulum

dynamics is provided in connection with the shallow water equations, with an emphasis on the approximate polygonal trajectories associated with atmospheric flows in polar regions of rotating planets.

2. Model of equatorial waves in a strip

Equatorial waves, which consist of eastward- and westward-moving disturbances, are oceanic and atmospheric waves confined near the equator. These waves can propagate in both zonal and meridional directions. Equatorial waves significantly influence climate phenomena such as El Niño (**33**, **34**) and Cromwell currents in deep surface layers (**35**).

Equatorial waves can be separated into subclasses based on their dynamics, taking into account their periods, speeds and directions of propagation. The well-known waves in the equatorial atmosphere are Kelvin, Rossby and inertia-gravity waves. Experimental evidence of equatorial waves was uncovered using various methods, such as spectral studies and satellite data analysis [see, for example (**29**, **36** to **41**)]. Initially regarded as a theoretical curiosity, the study of equatorial waves, rooted in the shallow water equations and Hermite functions, gained attention in the 1960s with direct measurements of equatorial mixed Rossby-gravity waves and Kelvin waves (**42** to **44**).

In this section, we provide the full analytical asymptotic solution of the linearised shallow water equations in a narrow band linked to atmospheric flows near the equatorial region. We also investigate the dispersion properties of equatorial waves by considering the combined effects of the rotating system in the presence of gravitational forces. The study presented in this section emphasises on the asymptotic analysis of continuum models for equatorial regions, analysing the dynamics of Kelvin, inertia-gravity and Rossby waves, by considering the refined meridional velocity equation. The refined version of the meridional equation, derived via the second-order asymptotic approximation procedure, is new, and the coefficient of Y^2 includes an additional term. Through this analysis, the eigenmodes and eigenfunctions for equatorial wave solutions are derived, which take into account the combined effects of the Coriolis force and gravity. Furthermore, the standing mode patterns for Rossby and inertia-gravity waves within equatorial channels are presented. In the appendix we discuss the dispersion characteristics of the harmonic wave solutions in comparison with the Matsuno model (**17**).

2.1. *Problem formulation of equatorial waves*

Given our focus on wave motions near the equator, we consider the linearised shallow water equations given by (1.1)–(1.3) and prescribe Dirichlet boundary conditions in the meridional direction for the velocity component v at $y = \pm a$, where a is an appropriate positive quantity. This condition is important for maintaining the validity of the equatorial approximation in our model. Thus, the following boundary conditions are prescribed on the boundaries of the equatorial region:

$$v\Big|_{y=\pm a} = 0. \tag{2.1}$$

In meteorology and oceanography, the spatial variation of the Coriolis parameter is of importance. The Coriolis parameter, given by $f = 2\Omega\sin(\phi)$, depends on the angular speed Ω and latitude ϕ. We approximate the Coriolis parameter with the latitude being linearly proportional to the distance from the equator, that is $\phi = y/R$, in the radian measure, where R denotes the radius of the Earth.

We look for time-harmonic solutions in the form of zonally propagating waves, given by

$$(u, v, h) = \mathrm{Re}\{(A(y), B(y), C(y))e^{i(kx+\omega t)}\}, \tag{2.2}$$

where k is the (zonal) wavenumber, ω is the radian frequency and $A(y), B(y)$ and $C(y)$ are functions describing the horizontal and transverse velocity components and height field component of the fluid. Substituting the above assumptions and given expressions into the system (1.1)–(1.3) results in a set of ordinary differential equations for A, B and C:

$$i\omega A(y) - 2\Omega \sin\left(\frac{y}{R}\right) B(y) = -igkC(y), \tag{2.3}$$

$$i\omega B(y) + 2\Omega \sin\left(\frac{y}{R}\right) A(y) = -g\frac{dC}{dy}, \tag{2.4}$$

$$i\omega C(y) + H\left(ikA(y) + \frac{dB}{dy}\right) = 0, \tag{2.5}$$

subject to the Dirichlet boundary conditions [see (2.1)]:

$$B(y)\Big|_{y=\pm a} = 0. \tag{2.6}$$

The above problem formulation in a finite-width equatorial strip differs from the analysis of the Weber-type equations in an infinite domain discussed in (**17**, **45**, **46**).

The solutions of the shallow water equations related to the Kelvin waves, with the dispersion equation $\omega^2 = gHk^2$, are discussed in Appendix A. To obtain other solutions of the shallow water equations we consider the case when $\omega^2 \neq gHk^2$. In this case, waves of two different types are obtained as solutions, which are referred to as the inertia-gravity wave and the Rossby wave. Re-arranging (2.5) for $C(y)$ and substituting into (2.3) yields the representations for the height field and zonal velocity components, respectively, in the form:

$$C(y) = i\frac{H(ikA(y) + \frac{\partial B}{\partial y})}{\omega}, \quad A(y) = -i\frac{(2\Omega\omega \sin\left(\frac{y}{R}\right)B(y) + gkH\frac{\partial B}{\partial y})}{\omega^2 - gHk^2}. \tag{2.7}$$

Upon substituting (2.7) into (2.4), we obtain the following second-order meridional velocity component equation together with the associated boundary conditions:

$$gH\omega\frac{d^2B}{dy^2} + \left[\omega^3 - gHk^2\omega - 4\Omega^2\omega\sin^2\left(\frac{y}{R}\right) + \frac{2gkH\Omega}{R}\cos\left(\frac{y}{R}\right)\right]B(y) = 0, \quad B(\pm a) = 0. \tag{2.8}$$

The above problem is an eigenvalue problem with the general solution consisting of a linear combination of confluent Heun functions [see, for example (**47**, **48**)]. Here, we consider the shallow water equations within a horizontal layer of fluid, where the flows are confined near the equator, that is within $-a \leq y \leq a$. Thus, we neglect higher-order terms in the expansions of $\sin(y/R)$ and $\cos(y/R)$. In particular, we present the asymptotic solutions for the eigenvalues and eigenfunctions of the equatorial waves for two different analytic approximations: first, by neglecting terms of order $O((y/R)^2)$, and second, by neglecting the terms of order $O((y/R)^3)$ in the meridional velocity

equation in (2.8). It is shown that the dispersion properties of inertia-gravity and Rossby waves are captured by both approximations, while the second approximation yields additional asymptotic terms in the solutions for the equatorial waves.

In the following analysis, it is convenient to introduce the dimensionless variables

$$\tilde{Y} = \frac{y}{R}, \quad \tilde{\omega} = \omega\sqrt{\frac{R}{g}}, \quad \tilde{k} = kR, \quad \tilde{\Omega} = 2\Omega\sqrt{\frac{R}{g}}, \quad \tilde{H} = \frac{H}{R}, \tag{2.9}$$

where the quantities with the symbol '∼' are dimensionless. Hence, we consider the non-dimensional form of the meridional velocity problem (2.8), given by (the symbol '∼' has been dropped for convenience)

$$\frac{d^2\hat{B}}{dY^2} + \left[\frac{\omega^2}{H} - k^2 - \frac{\Omega^2}{H}\sin^2(Y) + \frac{k\Omega}{\omega}\cos(Y)\right]\hat{B}(Y) = 0, \quad \hat{B}(\pm\epsilon) = 0, \tag{2.10}$$

where $\hat{B}(Y) = B(RY)$ and $\epsilon = a/R$. It is noted that $Y = \pm\epsilon$ correspond to the upper and lower boundaries of the strip.

2.2. *Asymptotic models of the meridional velocity equation*

2.2.1. Case 1: Dirichlet problem for the Weber-type differential equation. When third-order terms in the expansions of $\sin(Y)$ and $\cos(Y)$ are neglected in (2.10), we obtain the following boundary value problem:

$$\frac{d^2\hat{B}}{dY^2} + \left[\Lambda - \Phi Y^2\right]\hat{B}(Y) = 0, \quad \hat{B}(\pm\epsilon) = 0, \tag{2.11}$$

where

$$\Lambda = \frac{\omega^2}{H} - k^2 + \frac{k\Omega}{\omega}, \quad \Phi = \frac{\Omega^2}{H} + \frac{k\Omega}{2\omega}. \tag{2.12}$$

The differential equation shown in (2.11) seems to have first appeared in the paper (**49**). The above non-dimensional coefficients are fully consistent with the asymptotic expansions to the order $O(Y^2)$. The coefficient of Y^2 in (2.11), denoted by Φ, depends on the non-dimensional frequency ω and the non-dimensional wavenumber k. This coefficient is different from that in (**17**), where the order $O(Y^2)$ terms were missing due to the fact that the cosine term was approximated as a constant, which was an omission. When $\Lambda = 0$, the solutions are represented by the modified Bessel functions (**48**), whereas when $\Phi = 0$, the solutions can be written as a linear combination of sinusoidal functions. The boundary conditions at $Y = \pm\epsilon$ also capture the meridional velocity conditions for the waveforms in the equatorial band, which are also consistent with the problem assumptions. The analysis of the above meridional velocity equation is presented in Section 2.6.

2.2.2. Case 2: Harmonic oscillator model. If the terms of order $O(Y^2)$ are neglected in (2.10), we obtain a non-dimensional equation with constant coefficients resembling the well-known harmonic oscillator:

$$\frac{d^2\hat{B}}{dY^2} + \Lambda\hat{B}(Y) = 0, \quad \hat{B}(\pm\epsilon) = 0, \tag{2.13}$$

where the non-dimensional quantities Λ and ϵ are defined in (2.12) and Section 2.1, respectively. In this case, the solution for $\hat{B}(Y)$ consists of sinusoidal terms; an exact non-trivial solution which satisfies the boundary conditions at $Y = \pm\epsilon$ can be obtained, as detailed in Section 2.3. Quantitative comparisons between the dispersion properties of the harmonic waves in a bounded equatorial channel and those of the trapped equatorial waves in an unbounded channel, derived in (**17**), are presented in Appendix B.

2.3. *Harmonic waves in an equatorial channel*

In this section, the full analytical solution of the shallow water equations is presented by neglecting terms of order $O(Y^2)$. Accordingly, Dirichlet boundary conditions are imposed on the narrow equatorial channel. The corresponding eigenvalues and eigenfunctions of the equatorial waveforms are also analysed.

In the vicinity of the equator, by neglecting terms of order $O(Y^2)$ in the expansions of $\sin(Y)$ and $\cos(Y)$ in (2.10), the non-dimensional meridional velocity component equation takes the form (2.13). To obtain bounded non-trivial solutions of problem (2.13), we take $\Lambda > 0$, and look for solutions in the form

$$\hat{B}(Y) = b^{(1)}\cos(\sqrt{\Lambda}Y) + b^{(2)}\sin(\sqrt{\Lambda}Y), \tag{2.14}$$

where $b^{(1)}$ and $b^{(2)}$ are arbitrary constants. Applying the conditions at $Y = \pm\epsilon$, results in the following exact form of the meridional velocity component

$$\hat{B}_j(Y) = \begin{cases} b_j^{(1)}\cos(\sqrt{\Lambda_j}Y), & j = 1,3,5,\ldots, \\ b_j^{(2)}\sin(\sqrt{\Lambda_j}Y), & j = 2,4,6,\ldots, \end{cases} \tag{2.15}$$

where the solvability condition yields

$$\sqrt{\frac{\omega^2}{H} - k^2 + \frac{k\Omega}{\omega}} = \frac{j\pi}{2\epsilon}, \quad j = 1,2,3,\ldots. \tag{2.16}$$

Equation (2.16) is the non-dimensional dispersion relation, describing the connection between the non-dimensional frequency and non-dimensional zonal wavenumber for a chosen meridional mode j. For each j, there are generally three roots of the dispersion equation when H, k, Ω and ϵ are specified. In particular, two of the three roots of (2.16) correspond to inertia-gravity waves, while the third root to a Rossby wave as shown in Fig. 1. The region corresponding to $\Lambda > 0$ is shaded in Fig. 1. The representation of the meridional eigenfunction components (2.15) shows that the even modes ($j = 2,4,6,\ldots$) are skew-symmetric about the equatorial region and the odd modes ($j = 1,3,5,\ldots$) are symmetric.

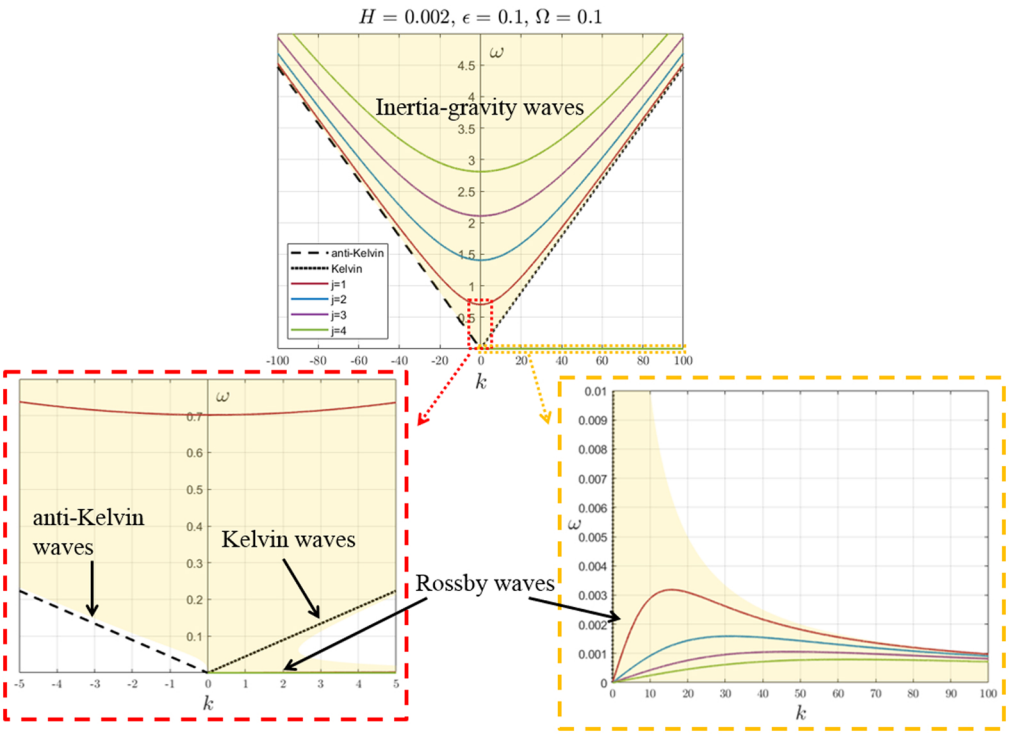

Fig. 1 Dispersion diagram for equatorial waves trapped in a narrow strip as a function of the non-dimensional frequency ω, and non-dimensional zonal wavenumber k. The non-dimensional parameter values are $H = 0.002, \epsilon = 0.1$ and $\Omega = 0.1$. The anti-Kelvin and Kelvin modes are described in Appendix A and Section 2.6. The remaining dispersion curves correspond to the solutions of (2.16). Inertia-gravity waves are represented by the high-frequency curves for the values $j = 1, 2, 3, 4$, resulting in westward- or eastward-propagating waveforms, while for the same values of j, the low-frequency curves denote the Rossby waves. The shaded region corresponds to $\Lambda > 0$.

The group velocity of the equatorial waves is calculated from the dispersion relation (2.16), and can be approximated by

$$\frac{d\omega}{dk} = \frac{H\omega(-2k\omega + \Omega)}{H\Omega k - 2\omega^3}. \tag{2.17}$$

Another useful property in the description of equatorial waves is the phase velocity, which is defined by ω/k, and indicates the speed at which the phase of the individual wave components propagate in the horizontal direction.

As noted previously, there are three main classes of equatorial waves in the narrow strip, which are inertia-gravity, Rossby and Kelvin waves. The meridionally bounded solutions in the south and north of the equatorial band introduce an additional mode: a non-dispersive, westward-propagating anti-Kelvin wave (**50** to **52**). It is noted that the values of the non-dimensional parameters Ω, H and

ϵ, results in only the eastward-propagating Kelvin mode to be situated in the shaded region, defined by $\Lambda > 0$ [where Λ is given in (2.12)], while the anti-Kelvin mode lies outside the shaded region (see Fig. 1). The inertia-gravity waves and Rossby waves are within the shaded area as shown in Fig. 1.

Taking into account (2.9) and substituting (2.15) into the non-dimensional forms of (2.7), yields the non-dimensional zonal velocity and height field components, respectively, as

$$\hat{A}_j(Y) = \begin{cases} -ib_j^{(1)} \frac{\Omega\omega \sin(Y)\cos(\sqrt{\Lambda_j}Y) - kH\sqrt{\Lambda_j}\sin(\sqrt{\Lambda_j}Y)}{\omega^2 - Hk^2}, & j = 1,3,5,\ldots, \\ -ib_j^{(2)} \frac{\Omega\omega \sin(Y)\sin(\sqrt{\Lambda_j}Y) + kH\sqrt{\Lambda_j}\cos(\sqrt{\Lambda_j}Y)}{\omega^2 - Hk^2}, & j = 2,4,6,\ldots, \end{cases} \tag{2.18}$$

and

$$\hat{C}_j(Y) = \begin{cases} ib_j^{(1)} H \frac{\Omega k \sin(Y)\cos(\sqrt{\Lambda_j}Y) - \omega\sqrt{\Lambda_j}\sin(\sqrt{\Lambda_j}Y)}{\omega^2 - Hk^2}, & j = 1,3,5,\ldots, \\ ib_j^{(2)} H \frac{\Omega k \sin(Y)\sin(\sqrt{\Lambda_j}Y) + \omega\sqrt{\Lambda_j}\cos(\sqrt{\Lambda_j}Y)}{\omega^2 - Hk^2}, & j = 2,4,6,\ldots, \end{cases} \tag{2.19}$$

where $\hat{A}_j(Y) = A_j(RY)$ and $\hat{C}_j(Y) = \sqrt{\frac{g}{R}} C_j(RY)$.

By introducing the additional variables $x = R\tilde{X}$ and $t = \sqrt{R/g}\tilde{T}$, where the quantities with the symbol '$\sim$' are dimensionless, and substituting the above expressions for $\hat{A}_j(Y), \hat{B}_j(Y)$ and $\hat{C}_j(Y)$ into (2.2), results in the dimensionless zonal and meridional velocities and height field representations as follows (dropping the '$\sim$' for convenience)

$$\begin{aligned} \hat{u}_j &= -\mathrm{Im}\{\hat{A}_j(Y)\}\sin(kX + \omega T), \\ \hat{v}_j &= \hat{B}_j(Y)\cos(kX + \omega T), \\ \hat{h}_j &= -\mathrm{Im}\{\hat{C}_j(Y)\}\sin(kX + \omega T). \end{aligned} \tag{2.20}$$

Equations (2.20) describe the zonally propagating Rossby and inertia-gravity waves in a narrow equatorial band. We also note that the above non-dimensional eigenfunctions differ from the Kelvin wave solutions presented in Appendix A.

In the subsequent section, we present examples of the eigenfunctions linked to the propagating inertia-gravity and Rossby waves, highlighting the zonal and meridional components of the zonal wave solutions.

2.4. *Eigenmodes of Rossby and inertia-gravity waves in an equatorial channel*

In Section 2.3, we have shown that the non-dimensional dispersion equation, given by (2.16), can be used to determine the frequencies and wavenumbers of the waveforms in a narrow equatorial band. Some examples of the eigenfunctions obtained in Section 2.3 are presented in this section, in connection with various dispersion characteristics of the different types of equatorial waves.

The non-dimensional eigenfunctions of the Kelvin waves, characterised by the zero meridional velocity component, are addressed in Appendix A. These waves are non-dispersive and are associated with wind stress anomalies, the Coriolis force, coastal boundaries and variations in sea surface height and temperature (**53**, **54**). Kelvin waves are integral to oceanic-atmospheric

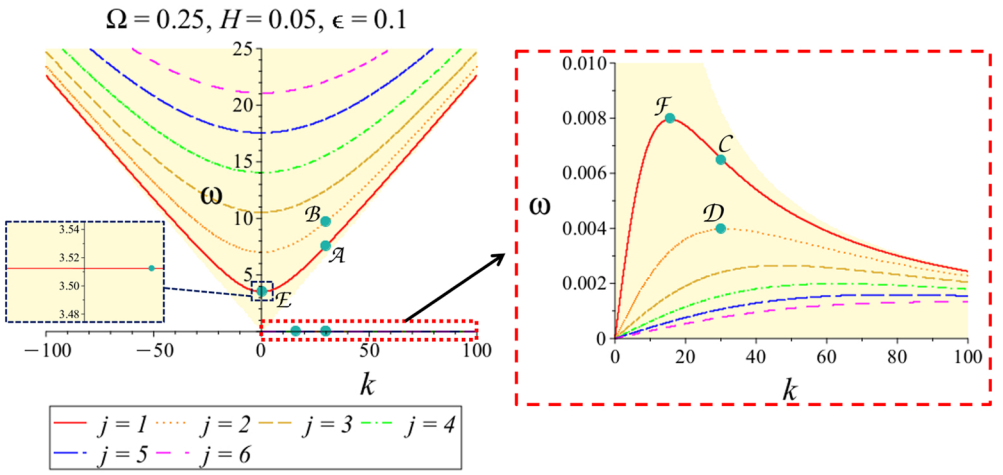

Fig. 2 Non-dimensional frequencies as functions of the non-dimensional wavenumbers defined by the dispersion relation (2.16) for a range of modes and the non-dimensional parameter values $\Omega = 0.25, H = 0.05$ and $\epsilon = 0.1$. The points labelled by $\mathcal{A}, \mathcal{B}, \mathcal{C}, \mathcal{D}, \mathcal{E}$ and $\mathcal{F}$, shown on the dispersion curves, correspond to the values of ω and k of the eigenfunctions for the equatorial modes described in the text

interactions and climate phenomena [see, for example (**55**)]. The low frequency modes shown in Fig. 2 correspond to the equatorial Rossby waves (also known as planetary waves), which propagate in the atmosphere and oceans. Such waves are characterised by their lower frequencies and longer wavelengths compared to Kelvin waves. At higher frequencies, the equatorial inertia-gravity waves are present, linked to the high-frequency curves displayed in Fig. 2; these waveforms can propagate in various directions. Analysing inertia-gravity waves and Rossby waves is crucial for understanding and predicting atmospheric and oceanic circulation patterns on regional and global scales.

2.4.1. Eigenfunctions of the zonally propagating equatorial wave solutions. The sinusoidal solutions of the shallow water equations, describing zonally propagating waves in a channel, have been derived in Section 2.3. The set of admissible non-dimensional frequencies ω, and non-dimensional zonal wavenumbers k, are defined according to the relation (2.16) for a positive integer value of j. In addition, for each j, the non-dimensional eigenfunctions of the inertia-gravity and Rossby modes are given by (2.20). From the analysis presented in Section 2.3 for inertia-gravity and Rossby waves, if follows that if j is an odd positive integer then $\hat{v}$ is an even function, and $\hat{u}$ and $\hat{h}$ are odd functions with respect to the non-dimensional variable Y. Conversely, if j is an even positive integer, the parities of the velocity and height fields are reversed.

In this section, we illustrate the non-dimensional eigenmodes of the equatorial waveforms in a narrow band, with the focus on the zonal and meridional velocity components. In each figure, one wavelength in the X-direction is shown. The group velocity, defined by (2.17), is used to determine the speed and direction of motion of the equatorial waves. In the illustrative examples, the wavenumbers are chosen as either $k = 30$ or $k = -30$ to observe one wavelength in the X-direction with a comparable order of magnitude to the meridional domain. Additionally, the equator runs through the centre of each diagram, with the horizontal boundaries at $Y = \pm\epsilon$. The change

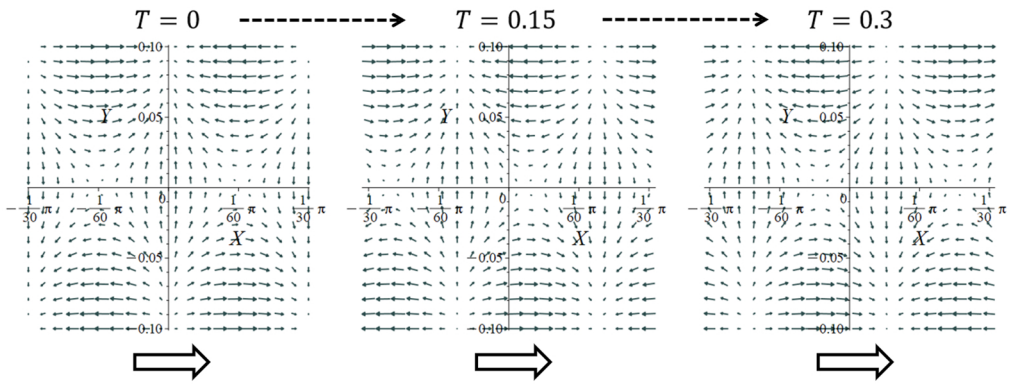

Fig. 3 Evolution of the eastward-propagating inertia-gravity eigenmode for the zonal and meridional velocity components at different normalised times corresponding to $j = 1$ (see Section 2.3). The eigenfunctions for the inertia-gravity wave are defined according to (2.20). The non-dimensional zonal wavenumber and non-dimensional frequency of the oscillations are respectively 30 and 7.5688. The arrows denote the direction of propagation of the waveforms

in frequency values of the waveforms correspond to different points on the dispersion curves. For each illustrative example presented in this section, the parameter values are $H = 0.05, \Omega = 0.25$ and $\epsilon = 0.1$.

The eigenfunctions for the zonal and meridional velocities of the eastward-moving inertia-gravity mode for $j = 1$ at various normalised time steps are shown in Fig. 3. The direction of the propagating waves is determined by the positive group velocity [see (2.17)], and is represented by the arrows in Fig. 3. Additionally, the non-dimensional wavenumber and non-dimensional frequency values are $k = 30$ and $\omega = 7.5688$, respectively, and correspond to the point $\mathcal{A}$ in Fig. 2. The eigenfunctions have the sinusoidal form derived in Section 2.3, reflecting the oscillatory behaviour of these waves in both the zonal and meridional directions. It is noted that westward-propagating inertia-gravity waves are obtained when $k = -30$ and $\omega = 7.5754$, where the waveforms travel in the negative X-direction. A positive group velocity corresponds to an eastward wave propagation, while a negative group velocity indicates a westward-propagating wave. The frequencies of the eastward- and westward-propagating waves differ due to the asymmetry of the inertia-gravity dispersion curves (see Fig. 2), as a result of the Coriolis force.

In Fig. 4, we present an example demonstrating the evolution of the eastward-propagating inertia-gravity wave for $j = 2$, with the zonal wavenumber $k = 30$ and frequency $\omega = 9.7113$. The corresponding dispersion diagram is shown in Fig. 2, with the associated point of the equatorial inertia-gravity mode denoted by $\mathcal{B}$. Compared to the eigenmodes illustrated in Fig. 3, the parities of the non-dimensional velocity components presented in Fig. 4 change: for $j = 1$, $\hat{v}$ and $\hat{u}$ are even and odd in Y, respectively, whereas for $j = 2$, $\hat{v}$ and $\hat{u}$ become odd and even in Y, respectively. In addition, the frequency of the inertia-gravity waves is higher in the example shown in Fig. 4 compared to Fig. 3. The eigenmodes shown in Fig. 4 also display a significant zonal velocity component along the centre of the equatorial band. Fundamental differences between the general structures of the inertia-gravity modes can also be observed. Furthermore, it is noted that eigenfunctions linked to the westward-propagating inertia-gravity waveforms also exist when $k = -30$ and $\omega = 9.7153$.

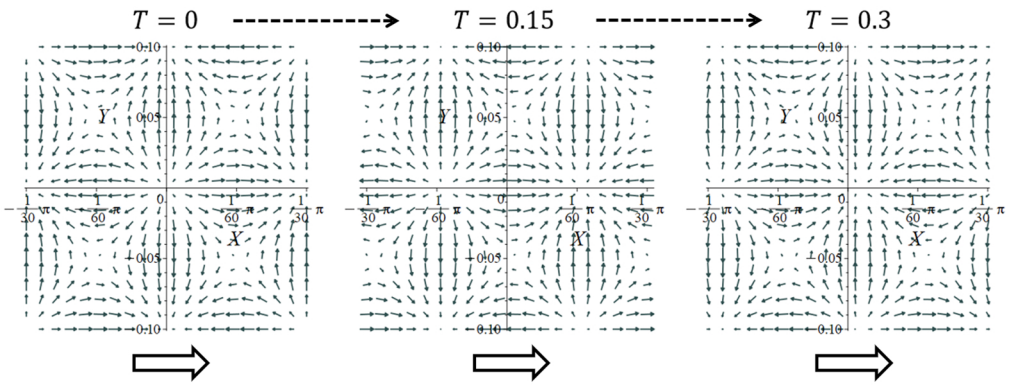

Fig. 4 Non-dimensional eigenmode for the eastward-propagating inertia-gravity waveform corresponding to $j = 2$, with the non-dimensional parameter values $\Omega = 0.25$, $H = 0.05$ and $\epsilon = 0.1$, and a selection of values for the non-dimensional time variable T. The non-dimensional wavenumber and non-dimensional frequency values are 30 and 9.7113, respectively

In Fig. 5, we present examples of the non-dimensional eigenfunctions of Rossby waves propagating in the narrow equatorial band for two different modes. Fig. 5(a) displays the westward-propagating Rossby wave for $j = 1$ with $(k, \omega) = (30, 0.0065)$, whereas Fig. 5(b) shows the eastward-propagating Rossby wave for the $j = 2$ mode with $(k, \omega) = (30, 0.0040)$. These points are denoted by $\mathcal{C}$ and $\mathcal{D}$ in the dispersion diagram in Fig. 2, and correspond to the low-frequency dispersion curves. Vortices are observed in the waveforms for both propagating Rossby modes, which differ from the inertia-gravity modes presented in Figs 3 and 4. As shown by the examples, higher modes corresponding to higher values of j result in an increase in the number of vortices for the Rossby modes (see Fig. 5) and greater meridional variations in the flow for the inertia-gravity modes (see Figs 3 and 4), associated with changes in zonal wavelengths, frequencies and energy distributions. Rossby waves are characterised by rotational flows, while inertia-gravity waves display a more divergent behaviour in connection with their shorter horizontal wavelengths and higher frequencies than Rossby waves. The dominant features of inertia-gravity waveforms in a continuum (for example eastward or westward propagation and asymmetric properties of the dispersion curves) are similar to the elastic chiral gravitational waves in a chiral discrete lattice strip presented in part 1.

2.4.2. Standing mode patterns for Rossby and inertia-gravity waves. Examples of standing mode patterns for both Rossby and inertia-gravity waves are presented in this section. Equatorial standing modes represent localised oscillations, and in such cases, the waveform patterns remain stationary in space. The standing modes of Rossby and inertia-gravity waves are characterised by the vanishing group velocity defined by (2.17).

There is a historical account of Kelvin waves and Rossby waves significantly influencing the dynamics of El Niño events, which may provide insights into the decline of ancient civilisations, such as the Moche civilisation in northern Peru in the late sixth century [see (**56**, **57**)]. The climate record suggested that the environmental changes likely included a mega El Niño that caused 30years of intense rain and flooding on the coast, followed by 30years of drought (**56**, **58**). The

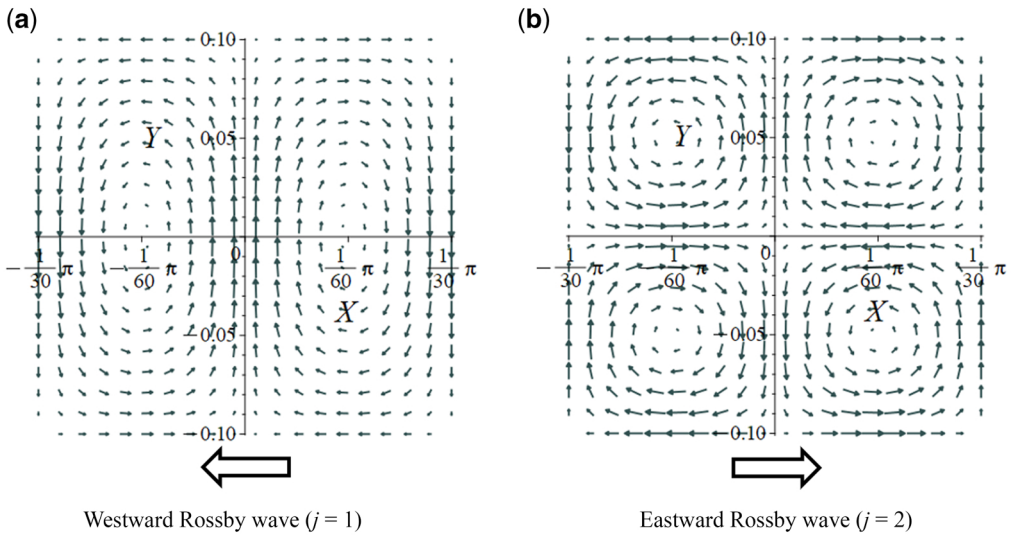

Fig. 5 Eigenfunctions of the non-dimensional velocity components, given by (2.20), of the Rossby modes for $j = 1$ and $j = 2$ in parts (a) and (b), respectively; (a) westward-propagating Rossby wave for $(k,\omega) = (30, 0.0065)$ and (b) eastward-propagating Rossby wave for $(k,\omega) = (30, 0.0040)$. The arrows indicate the direction of the wave propagation

atmospheric standing waves, particularly the equatorial Rossby waves (**59** to **61**), modulated by oceanic conditions could explain the long-term climate impacts experienced during a mega El Niño event. These extreme weather phenomena disrupted the Moche way of life and damaged irrigation systems leading to the collapse of the Moche civilisation [see, for example (**56**, **62** to **65**)].

Standing wave patterns, described by the non-dimensional eigenfunctions (2.20) for $j = 1$, corresponding to inertia-gravity and Rossby waves are shown in Fig. 6(a) and (b), respectively. Similarly to the eigenmode diagrams shown in Section 2.4.1, the eigenfunctions in Fig. 6 are plotted for one wavelength in the X-direction. We note that although the group velocities of the waveforms are zero, the phase velocities in both presented examples are positive, indicating that the phase of the wave is moving in the positive X-direction. Furthermore, standing wave modes with negative phase velocities and zero group velocities can also be obtained with a suitable value of the non-dimensional parameter Ω. The presence of the Coriolis force results in asymmetric dispersion curves for the inertia-gravity waves, leading to standing modes with non-zero wavenumbers k [see Fig. 6(a)]. For higher modes, additional vortices are observed for the standing Rossby modes, and greater meridional variations are noticed in the standing inertia-gravity modes.

2.5. *Modes of the meridional velocity equation*

In this section, we consider the non-dimensional linearised shallow water equations for a horizontal layer of fluid, where the meridional velocity component is described by the Weber-type differential equation (**48**, **66**, **67**).

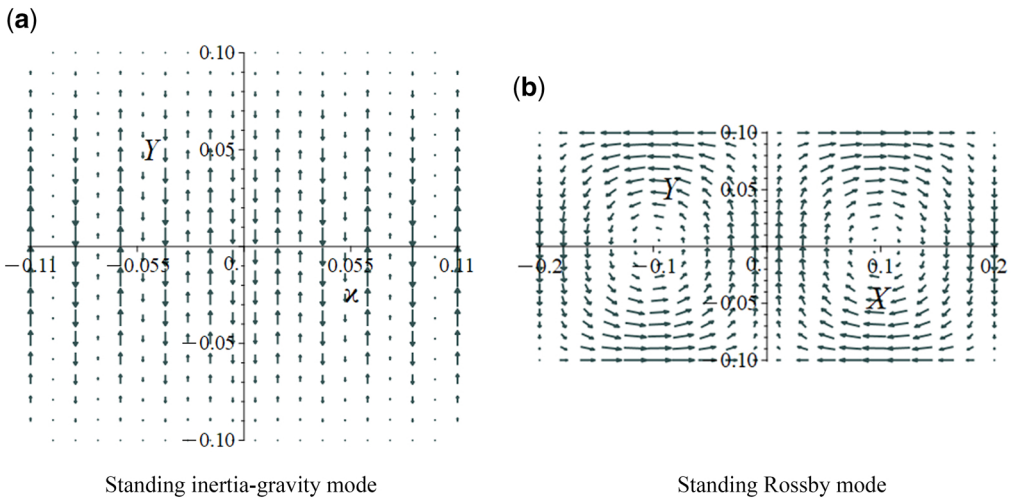

Fig. 6 Standing inertia-gravity and Rossby modes for $j = 1$, with the parameter values $\Omega = 0.25$, $H = 0.05$ and $\epsilon = 0.1$. The associated dispersion diagram is shown in Fig. 2, with the points $\mathcal{E}$ and $\mathcal{F}$ corresponding to the standing modes in parts (a) and (b), respectively. (a) Standing inertia-gravity wave for $(k, \omega) = (0.0356, 3.5124)$ with the horizontal scaling $X = 8 \times 10^2 \chi$, and (b) standing Rossby wave for $(k, \omega) = (15.7079, 0.0080)$.

When third-order terms in the expansions of $\sin(Y)$ and $\cos(Y)$ are neglected in (2.10), we obtain the following meridional velocity equation (see Section 2.2.1):

$$\frac{d^2\hat{B}}{dY^2} + \left[\Lambda - \Phi Y^2\right]\hat{B} = 0, \quad \hat{B}(Y = \pm\epsilon) = 0, \tag{2.21}$$

where Λ and Φ are defined in (2.12), and depend on the non-dimensional frequency and non-dimensional zonal wavenumber. The case of $\Phi = 0$ was discussed in Section 2.3.

We consider the solutions to the problem (2.21) subject to the conditions

$$\Lambda > 0, \quad \Phi > 0. \tag{2.22}$$

(We assume that the non-dimensional quantities H and Ω (see Section 2.1) satisfy the condition $\Omega/\sqrt{H} > 1/2$, which holds for the corresponding dimensional parameters on the Earth. Based on the analysis of harmonic waves presented in Section 2.3, we also take $\Lambda > 0$. Then, it follows that $\frac{\Omega}{2\omega} - \sqrt{\frac{\omega^2}{H} + \frac{\Omega^2}{4\omega^2}} < k < \frac{\Omega}{2\omega} + \sqrt{\frac{\omega^2}{H} + \frac{\Omega^2}{4\omega^2}}$, and taking into account (2.12), it can be deduced that $\Phi = \frac{\Omega^2}{H} + \frac{k\Omega}{2\omega} > \frac{\Omega^2}{H} + \frac{\Omega^2}{4\omega^2} - \frac{\Omega}{2\omega}\sqrt{\frac{\omega^2}{H} + \frac{\Omega^2}{4\omega^2}} = \frac{\Omega^2(\omega^2(4\Omega^2 - H) + 2H\Omega^2)}{4H^2\omega^2\left(\frac{\Omega^2}{H} + \frac{\Omega^2}{4\omega^2} + \frac{\Omega}{2\omega}\sqrt{\frac{\omega^2}{H} + \frac{\Omega^2}{4\omega^2}}\right)} > 0.$)

The system (2.21) represents an equatorial wave problem for the meridional velocity component, and its solutions are given by a linear combination of parabolic cylinder functions [see for example

(**48**, **51**, **66**)] as follows

$$\hat{B}(Y) = \mathscr{C}_1 U\left(-\frac{\Lambda}{2\sqrt{\Phi}}, \sqrt{2}\Phi^{1/4}Y\right) + \mathscr{C}_2 V\left(-\frac{\Lambda}{2\sqrt{\Phi}}, \sqrt{2}\Phi^{1/4}Y\right), \tag{2.23}$$

where $\mathscr{C}_1$ and $\mathscr{C}_2$ are arbitrary constants, while U and V denote the parabolic cylinder functions (**48**, **67**), which form two linearly independent solutions of the differential equation shown in (2.21).

Applying the boundary conditions at $Y = \pm\epsilon$ results in the following non-dimensional dispersion relation:

$$\begin{aligned} &U\left(-\frac{\Lambda}{2\sqrt{\Phi}}, -\sqrt{2}\Phi^{1/4}\epsilon\right) V\left(-\frac{\Lambda}{2\sqrt{\Phi}}, \sqrt{2}\Phi^{1/4}\epsilon\right) \\ &\quad - U\left(-\frac{\Lambda}{2\sqrt{\Phi}}, \sqrt{2}\Phi^{1/4}\epsilon\right) V\left(-\frac{\Lambda}{2\sqrt{\Phi}}, -\sqrt{2}\Phi^{1/4}\epsilon\right) = 0. \end{aligned} \tag{2.24}$$

When the condition (2.24) is satisfied, there exist non-trivial solutions for the meridional velocity problem (2.21). Noting the representation (2.12), the equation (2.24) can be solved numerically yielding approximate non-dimensional eigenvalues associated with the equatorial waveforms. Moreover, since the boundary value problem (2.21) is of the Sturm-Liouville form, the eigenvalues form a non-negative increasing sequence in the interval $[-\epsilon, \epsilon]$. The derivation of the asymptotic solutions of the non-dimensional dispersion equation (2.24) can be found in Appendix C, where it is shown that the leading order terms of the solutions correspond to the solutions of the dispersion equation (2.16) of the harmonic equatorial waves.

In the papers (**16**, **17**, **29**), a dispersion equation was derived for the equatorial waves with the boundary conditions applied at infinity, where the propagating solutions were assumed to decay away from the equatorial region.

To obtain analytical insights into the solution of the eigenvalue problem (2.21), we construct an asymptotic approximation of the eigenfunctions and corresponding eigenvalues.

2.6. *Regular perturbation of the Weber-type equation describing the equatorial modes*

In this section, we derive the asymptotic approximations of the eigenfunctions and eigenvalues of the meridional velocity mode, corresponding to the Weber-type differential equation described in the previous section.

We examine approximations to the solutions by considering the problem (2.21) as a perturbation eigenvalue problem in the form

$$-\hat{B}_n''(Y) + \Phi Y^2 \hat{B}_n(Y) = \Lambda_n \hat{B}_n(Y), \quad \hat{B}_n(\pm\epsilon) = 0, \tag{2.25}$$

where $\Phi > 0$ and $\Lambda > 0$. Introducing the variables:

$$\xi = \frac{\pi Y}{2\epsilon}, \quad \Psi = \left(\frac{2\epsilon}{\pi}\right)^4 \Phi, \quad \lambda = \left(\frac{2\epsilon}{\pi}\right)^2 \Lambda, \tag{2.26}$$

the eigenvalue problem (2.25) can be re-written as

$$-\mathscr{B}_n''(\xi) + \Psi\xi^2 \mathscr{B}_n(\xi) = \lambda_n \mathscr{B}_n(\xi), \quad \mathscr{B}_n\left(\pm\frac{\pi}{2}\right) = 0, \tag{2.27}$$

where $\mathcal{B}_n(\xi) = \hat{B}_n\left(\frac{2\epsilon}{\pi}\xi\right)$. We derive an asymptotic solution for the eigenvalue problem (2.27) for the small perturbation parameter Ψ. The eigenfunctions $\mathcal{B}_n(\xi)$ and eigenvalues λ_n are sought in the asymptotic forms

$$\begin{aligned} \mathcal{B}_n(\xi) &= \mathcal{B}_n^{(0)}(\xi) + \Psi\mathcal{B}_n^{(1)}(\xi) + O(\Psi^2), \\ \lambda_n &= \lambda_n^{(0)} + \Psi\lambda_n^{(1)} + O(\Psi^2), \end{aligned} \tag{2.28}$$

where $\mathcal{B}_n^{(0)}(\xi)$ and $\lambda_n^{(0)}$ are the normalised eigenfunction and eigenvalue of the limit problem (2.27) when $\Psi = 0$, respectively, and $\mathcal{B}_n^{(1)}(\xi)$ and $\lambda_n^{(1)}$ are the correction terms.

2.6.1. The limit eigenvalue problem. The limit problem of the regular perturbation problem (2.27) takes the form

$$(\mathcal{B}_n^{(0)}(\xi))'' + \lambda_n^{(0)}\mathcal{B}_n^{(0)}(\xi) = 0, \quad \mathcal{B}_n^{(0)}\left(\pm\frac{\pi}{2}\right) = 0. \tag{2.29}$$

The eigenvalues and normalised eigenfunctions of the above problem are, respectively, given by

$$\lambda_n^{(0)} = n^2, \quad n = 1,2,3,\ldots, \tag{2.30}$$

and

$$\mathcal{B}_n^{(0)}(\xi) = \begin{cases} \sqrt{2/\pi}\cos(n\xi), & \text{for } n \text{ odd}, \\ \sqrt{2/\pi}\sin(n\xi), & \text{for } n \text{ even}. \end{cases} \tag{2.31}$$

The above solution corresponds to the meridional velocity mode component for the harmonic waves in a narrow equatorial band, as discussed in Section 2.3. It is noted that the solutions of the limit eigenvalue problem also lead to the eigenfunctions in the sinusoidal form. To simplify our analysis, we re-write the expression (2.31) as follows

$$\mathcal{B}_n^{(0)}(\xi) = \sqrt{\frac{2}{\pi}}\left(\frac{(1+(-1)^n)}{2}\sin(n\xi) + \frac{(1-(-1)^n)}{2}\cos(n\xi)\right), \quad n = 1,2,3,\ldots. \tag{2.32}$$

2.6.2. Evaluation of the first-order correction terms for the eigenfunctions and the eigenvalues. By substituting the asymptotic forms of the eigenfunction and eigenvalue (2.28) into (2.27) and using the above representations for the normalised eigenfunction and eigenvalue of the limit eigenvalue problem, it follows that the correction terms $\mathcal{B}_n^{(1)}$ and $\lambda_n^{(1)}$ satisfy the boundary value problem

$$(\mathcal{B}_n^{(1)}(\xi))'' + n^2\mathcal{B}_n^{(1)}(\xi) = -\lambda_n^{(1)}\mathcal{B}_n^{(0)}(\xi) + \xi^2\mathcal{B}_n^{(0)}(\xi), \quad \mathcal{B}_n^{(1)}\left(\pm\frac{\pi}{2}\right) = 0. \tag{2.33}$$

We look for solutions of the inhomogeneous problem (2.33) in the form

$$\mathcal{B}_n^{(1)}(\xi) = \sum_{j=1}^{\infty} a_{nj}\mathcal{B}_j^{(0)}(\xi) = \sqrt{\frac{2}{\pi}}\sum_{j=1}^{\infty} a_{nj}\left[\frac{(1+(-1)^j)}{2}\sin(j\xi) + \frac{(1-(-1)^j)}{2}\cos(j\xi)\right]. \tag{2.34}$$

By taking into account the forms of $\mathcal{B}_n^{(0)}(\xi)$ and $\lambda_n^{(0)}$ in Section 2.6.1 and the above representation for $\mathcal{B}_n^{(1)}(\xi)$, the differential equation in (2.33) can be written as

$$\sum_{j=1}^{\infty}(n^2-j^2)a_{nj}\mathcal{B}_j^{(0)}(\xi)=-\lambda_n^{(1)}\mathcal{B}_n^{(0)}(\xi)+\xi^2\mathcal{B}_n^{(0)}(\xi). \tag{2.35}$$

We note the orthogonality relations of the sinusoidal functions in $\mathcal{B}_j^{(0)}(\xi)$:

$$\int_{-\frac{\pi}{2}}^{\frac{\pi}{2}}\mathcal{B}_j^{(0)}(\xi)\mathcal{B}_p^{(0)}(\xi)d\xi=\delta_{jp}, \tag{2.36}$$

where p is a positive integer and δ_{jp} is the Kronecker delta function. As a result, multiplying (2.35) by $\mathcal{B}_p^{(0)}(\xi)$ and integrating over the interval $\left(-\frac{\pi}{2},\frac{\pi}{2}\right)$, yields the following

$$a_{np}(n^2-p^2)=\int_{-\frac{\pi}{2}}^{\frac{\pi}{2}}(-\lambda_n^{(1)}+\xi^2)\mathcal{B}_n^{(0)}(\xi)\mathcal{B}_p^{(0)}(\xi)d\xi. \tag{2.37}$$

When $p=n$, we obtain the eigenvalue $\lambda_n^{(1)}$:

$$\lambda_n^{(1)}=\int_{-\frac{\pi}{2}}^{\frac{\pi}{2}}\xi^2(\mathcal{B}_n^{(0)}(\xi))^2d\xi=\frac{\pi^2}{12}-\frac{1}{2n^2},\quad n=1,2,3,\ldots. \tag{2.38}$$

In particular, if $p\neq n$, we derive the coefficients a_{np}:

$$a_{np}=\frac{1}{n^2-p^2}\int_{-\frac{\pi}{2}}^{\frac{\pi}{2}}(-\lambda_n^{(1)}+\xi^2)\mathcal{B}_n^{(0)}(\xi)\mathcal{B}_p^{(0)}(\xi)d\xi=\frac{4np(-1)^{\frac{n+p}{2}}}{(n^2-p^2)^3}((-1)^n+(-1)^p). \tag{2.39}$$

To obtain the remaining coefficients a_{nn}, we normalise $\mathcal{B}_n(\xi)$ so that

$$\int_{-\frac{\pi}{2}}^{\frac{\pi}{2}}\mathcal{B}_n^2(\xi)d\xi=1. \tag{2.40}$$

Then since

$$\mathcal{B}_n^2(\xi)=(\mathcal{B}_n^{(0)}(\xi))^2+2\Psi\mathcal{B}_n^{(0)}(\xi)\mathcal{B}_n^{(1)}(\xi)+O(\Psi^2), \tag{2.41}$$

and

$$\int_{-\frac{\pi}{2}}^{\frac{\pi}{2}}(\mathcal{B}_n^{(0)}(\xi))^2d\xi=1, \tag{2.42}$$

it follows that

$$\int_{-\frac{\pi}{2}}^{\frac{\pi}{2}}\mathcal{B}_n^{(0)}(\xi)\mathcal{B}_n^{(1)}(\xi)d\xi=0. \tag{2.43}$$

Finally, (2.34), (2.36) and (2.43) yield the following

$$\int_{-\frac{\pi}{2}}^{\frac{\pi}{2}} \mathcal{B}_n^{(0)}(\xi)\left(\sum_{j=1}^{\infty} a_{nj}\mathcal{B}_j^{(0)}(\xi)\right)d\xi = 0, \tag{2.44}$$

which implies that $a_{nn} = 0$.

2.6.3. Asymptotic approximation of the dispersion relation. In this section, we derive the non-dimensional eigenvalues associated with the frequencies of the equatorial waveforms.

The asymptotic form of the eigenvalues is given by (see previous section)

$$\lambda_n = n^2 - \frac{1}{2n^2}\Psi + \frac{\pi^2}{12}\Psi + O(\Psi^2), \quad n = 1,2,3,\ldots. \tag{2.45}$$

Noting the variables (2.26), the above equation can be re-written as

$$\Lambda = \frac{n^2\pi^2}{4\epsilon^2} + \frac{\epsilon^2}{3}\Phi - \frac{2\epsilon^2}{n^2\pi^2}\Phi + O\left(\left(\frac{2\epsilon}{\pi}\right)^6\Phi^2\right). \tag{2.46}$$

Then by substituting the representations of Λ and Φ in terms of the non-dimensional frequency ω and non-dimensional wavenumber k, defined in (2.12), into (2.46), we obtain the following asymptotic dispersion equation:

$$\frac{\omega^2}{H} - k^2 + \frac{k\Omega}{\omega} = \frac{n^2\pi^2}{4\epsilon^2} + \epsilon^2\left(\frac{\Omega^2}{H} + \frac{k\Omega}{2\omega}\right)\left(\frac{1}{3} - \frac{2}{n^2\pi^2}\right), \quad n = 1,2,3,\ldots, \tag{2.47}$$

where the non-dimensional quantities Ω and H are defined in Section 2.1. The dispersion equation (2.16) in Section 2.3 is a first-order approximation of the above dispersion relation. Analytical insights of (2.47) are provided below. The above dispersion relation can also be derived by considering approximations of the parabolic cylinder functions in (2.24) as detailed in Appendix C.

2.6.4. Dispersion properties: waves parallel to an equatorial band. We present the asymptotic solutions of the dispersion equation (2.47), providing an analytic approximation of the non-dimensional frequencies for the propagating waves in a narrow equatorial band. Approximations of the non-dimensional eigenvalues for equatorial waves in an asymmetric channel were presented in (**51**).

Similar to the non-dimensional dispersion relation derived in Section 2.3, here we also observe that there are three roots of the dispersion equation (2.47) when H, k, Ω and ϵ are specified for a given mode n: two roots corresponding to inertia-gravity waves and the third to a Rossby wave. The solutions of (2.47) corresponding to a fixed $n \geq 1$ result in the dispersion curves displayed in Fig. 7, where the shaded region is defined by the conditions (2.22). In particular, we note that the even-numbered modes ($n = 2,4,6,\ldots$) of the normalised eigenfunctions derived above are skew-symmetric about the narrow equatorial region, while the odd-numbered modes ($n = 1,3,5,\ldots$) are symmetric. This behaviour is consistent with the eigenfunctions of the harmonic waves detailed

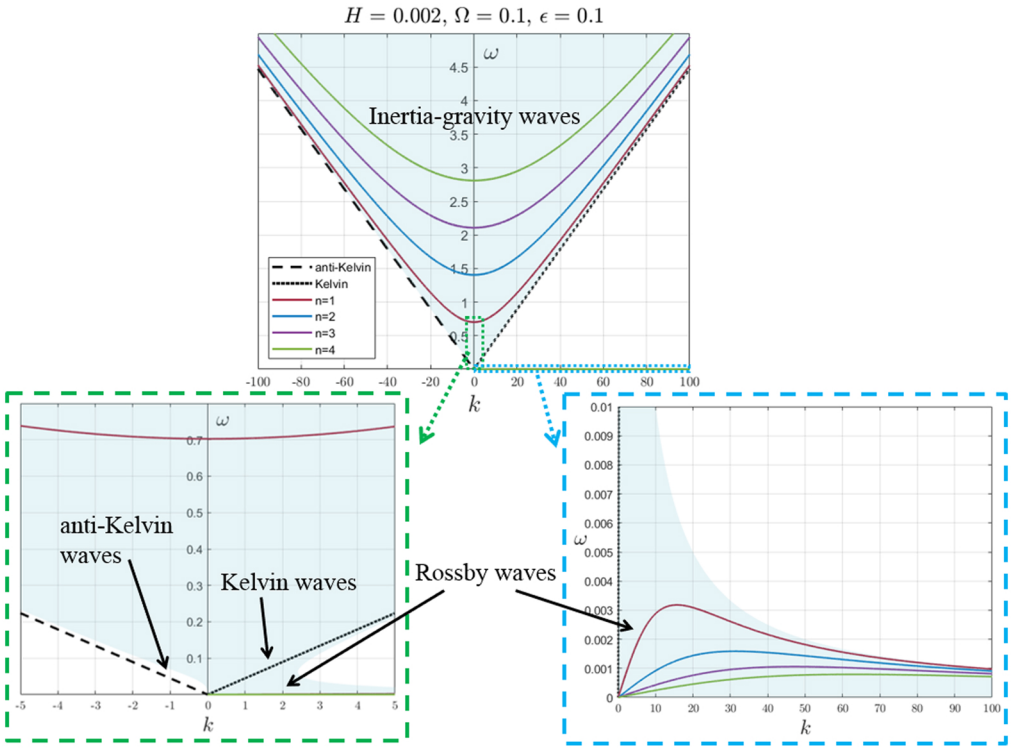

Fig. 7 The dispersion diagram corresponding to the non-dimensional dispersion relation (2.47) for $n = 1, 2, 3$ and 4, and the dimensionless parameters $\Omega = 0.1, H = 0.002$ and $\epsilon = 0.1$. For each value of n, the low-frequency Rossby waves and the high-frequency inertia-gravity are observed, which are situated within the shaded region corresponding to $\Lambda > 0$ and $\Phi > 0$ (see Section 2.5). The non-dispersive anti-Kelvin and Kelvin waves described in Appendix A are also shown; these are defined by the non-dimensional dispersion relation (A.6). The curve associated with the anti-Kelvin mode is outside the shaded region defined by (2.22)

in Section 2.3. The eigenfunctions of such equatorial modes are also discussed in (**50**, **51**, **68**), in the context of meridionally bounded propagating waves. The set of dispersion curves shown in Fig. 7 also form a collection of non-intersecting high-frequency inertia-gravity waves and low-frequency Rossby waves that are inside the shaded region, which can be compared to the curves in the dispersion diagram shown in Fig. 1. The main properties of these curves were also captured by the non-dimensional dispersion relation detailed in Section 2.3.

Taking into account the above analysis and computations, we identify the equatorial wave classes as follows:

- The anti-Kelvin and Kelvin waves that propagate zonally non-dispersively westward and eastward, respectively, in the narrow equatorial band with the normalised phase speed $\sqrt{H}$ (see Appendix A). The corresponding group velocities for the eastward- and westward-propagating

waveforms are given by $\pm\sqrt{H}$, respectively. We note that for increasing values of Y, the westward-propagating anti-Kelvin waves have zonally increasing amplitudes, while the eastward-propagating Kelvin waves are trapped in the narrow band with maximum amplitudes at the equator. The values of the non-dimensional parameters Ω, H and ϵ, together with the conditions (2.22), resulted in the dispersion curve of the anti-Kelvin mode being located outside the shaded region as shown in Fig. 7.

- For the high-frequency inertia-gravity waves for large k, the dispersion relation (2.47) yields the approximate non-dimensional frequencies, valid to $O(1/k)$,

$$\omega_{1,2} = \mp k\sqrt{H} - \frac{\Omega}{2k} \mp \frac{n^2\pi^2\sqrt{H}}{8k\epsilon^2} + \frac{\Omega(n^2\pi^2 - 6)(H \mp 2\Omega\sqrt{H})}{12Hn^2\pi^2 k}\epsilon^2, \quad n = 1,2,3.... \tag{2.48}$$

The above approximate roots correspond to the equatorial modes associated with the westward- and eastward- propagating inertia-gravity waves, as illustrated in Fig. 7. We note that the dispersion curves of the inertia-gravity waves are asymmetric relative to the vertical frequency axis due to the presence of the Coriolis force. The asymmetry becomes more evident for larger values of $|\Omega|$, and reversing the sign of Ω results in a change in the directional horizontal shift of the dispersion curves. Additionally, such asymmetry feature allows for short-period inertia-gravity waves with zonal phase velocities in opposite directions compared to the group velocities. An analogous asymmetry in the dispersion curves was also observed in part 1 for the infinite discrete chiral lattice strip subjected to gravity, where gyroscopic forces were present instead of the Coriolis force.

- Low-frequency Rossby waves for large k can be approximated by the following, valid to $O(1/k)$,

$$\omega_3 = \frac{\Omega}{k} - \frac{(n^2\pi^2 - 6)\Omega}{6n^2\pi^2 k}\epsilon^2, \quad n = 1,2,3.... \tag{2.49}$$

By neglecting terms of order $O(\epsilon^2)$, the representation (2.49) shows that the non-dimensional zonal wavenumber k is positive (*resp*. negative) for $\Omega > 0$ (*resp*. $\Omega < 0$). Thus, the phase velocities of the low-frequency Rossby waves in the equatorial band result in eastward-moving oscillations (*resp*. westward-moving oscillations) for $\Omega > 0$ (*resp*. $\Omega < 0$). The Rossby dispersion curves are presented in Fig. 7, where it is observed that although the phase velocity of the wave components corresponds to eastward-propagating disturbances for $\Omega > 0$ (*resp*. westward-propagating for $\Omega < 0$), their zonal group velocity can result in either eastward- or westward-propagating waves.

The above asymptotic analysis shows that the low-frequency Rossby waves can exhibit eastward (*resp*. westward) phase disturbances and westward (*resp*. eastward) wave propagations for $\Omega > 0$ (*resp*. $\Omega < 0$) and large k. Kelvin waves, being non-dispersive, move with phase disturbances at the same speed as their group velocity as detailed in Appendix A. Moreover, inertia-gravity waves can have either eastward or westward phase velocities, as well as either eastward or westward group velocities. For low zonal wavenumbers, the direction of the propagating inertia-gravity waves can vary due to the Coriolis force affecting the phase and group velocities. It is know that inertia-gravity waves propagate much faster than Rossby waves [see, for example (**17**, **50**, **69**)].

3. Gyropendulum approximation of the shallow water equations

In this section, we show that a gyropendulum [see, for example (**11**)] can be used to approximately describe the dynamics of a shallow water ridge in the polar regions of rotating planets. In this

approximation, the shallow water equations are considered at high latitudes, where the large magnitude of the Coriolis force contributes to the formation and motion of polar vortices. The articles (**70**, **71**) present the problem of the hexagonal jet stream at the polar region of Saturn as an unexplained challenge. In particular, the quote from (**70**), related to the interpretation of numerical simulations, reads as follows: 'Imagine we have a rubber band and we place a bunch of smaller rubber bands around it and then we just squeeze the entire thing from the outside. That central ring is going to be compressed by some inches and form some weird shape with a certain number of edges. That's basically the physics of what's happening. We have these smaller storms and they're basically pinching the larger storms at the polar region and since they have to coexist, they have to somehow find a space to basically house each system. By doing that, they end up making this polygonal shape'. Although this explanation may look satisfactory for some, in the present section we show that the essence of the observed effect is the combined contribution from the rotation of the planet and gravity. We also provide a simple asymptotic approximation, based on the gyropendulum model, which gives an approximate polygonal shape of the polar jet stream. We demonstrate that starting with a linearised form of the shallow water equations and assuming a purely horizontal flow, one obtains a system of equations resembling the governing equations of an elementary gyropendulum.

The analysis presented in this section provides a new framework for modelling the dynamics of the rotating fluid ridge. In this case, for a fluid particle, the restoring force, which includes gravity, returns the particle to its equilibrium position, while the Coriolis force, resulting from the planet's rotation, acts perpendicular to the particle's velocity in the rotating frame of reference. Conversely, for a gyropendulum, the restoring force arises due to gravity, whereas rotational effects are introduced through a gyroscopic spinner. Although Coriolis and gyroscopic forces emerge from distinct physical phenomena, they both induce analogous effects that influence the motions of structures in rotating systems. This characteristic forms a fundamental basis for our analysis.

We will also present typical examples of the gyropendulum trajectories approximating polygonal shapes by following the method presented in (**11**). The approximate polygonal trajectories, described by the combined action of gyroscopic forces and gravity, are linked to a range of natural phenomena at different scales, such as polygonal shapes in a partially filled cylindrical container subjected to a rotating bottom plate [see for example, (**72** to **74**)] or polygonal patterns in polar observations of rotating planets (**75** to **78**). The illustrative examples of the gyropendulum motions with polygonal approximations are presented in connection with polar jet streams on rotating celestial bodies.

3.1. *Transient motion of a gyropendulum and shallow water ridge*

The equations of motion for a linearised shallow water system in the vicinity of the South Pole of the Earth are written as (see Sections 1 and 2)

$$\frac{\partial u}{\partial t} + 2\Omega v = -g\frac{\partial h}{\partial x}, \quad \frac{\partial v}{\partial t} - 2\Omega u = -g\frac{\partial h}{\partial y}. \tag{3.1}$$

It is noted that changing the sign of Ω results in the corresponding shallow water model at the North Pole and thus, without loss of generality we only consider the system at the South Pole.

We investigate the motion of a polar ridge of fluid of constant density, subjected to a clockwise orientation, which is described by the linearised shallow water equations. In our model, we assume that the height deviation h, from the undisturbed fluid surface is negligibly small compared to the fluid depth H (see Section 1). Then, the fluid element corresponding to the maximum elevation of the perturbed surface can be represented by a ridge. In the following, we show that the motion

of the fluid ridge can be approximated by the linearised motion of an elementary gyropendulum. Accordingly, at the fluid height h, the flow is approximated as planar. With reference to the above assumptions, we note the following:

$$\frac{\partial h}{\partial x} = \frac{\mathcal{U}}{L}, \quad \frac{\partial h}{\partial y} = \frac{\mathcal{V}}{L}, \tag{3.2}$$

where $\mathcal{U}$ and $\mathcal{V}$ are the planar displacement components of the fluid particle at the tip of the ridge in the x- and y-directions, respectively, and L is defined as a characteristic length corresponding to the length of the gyropendulum arm. For the velocity components u and v along the vortex ridge, we use the approximation

$$u = \frac{d\mathcal{U}}{dt}, \quad v = \frac{d\mathcal{V}}{dt}. \tag{3.3}$$

Substituting the representations (3.2) and (3.3) into the system (3.1), in the linearised approximation, we deduce the system of coupled differential equations

$$\frac{d^2\mathcal{U}}{dt^2} + 2\Omega\frac{d\mathcal{V}}{dt} + g\frac{\mathcal{U}}{L} = 0, \quad \frac{d^2\mathcal{V}}{dt^2} - 2\Omega\frac{d\mathcal{U}}{dt} + g\frac{\mathcal{V}}{L} = 0. \tag{3.4}$$

The system (3.4) is analogous to the governing equations of a gyropendulum (**11**), describing the linearised motion of a pendulum, that swings under gravity, attached to a rotating spinner. Hence, the shallow water equations subject to the above assumptions provide a connection with the motion of a gyropendulum. We note that the gyropendulum approximation captures some aspects of the shallow water model, but it does not fully account for the complexity of the fluid dynamics. A detailed model of such phenomena would require a comprehensive CFD analysis. The system (3.4) also describes the trajectory of a Foucault pendulum and the motion of a particle moving on a rotating surface [see, for example (**79**, **80**)].

In (**11**, **23**), it was demonstrated that by selecting appropriate initial conditions and physical parameters, the moving gyropendulum can trace a predetermined polygonal trajectory. The full classification of the gyropendulum trajectories is also provided in (**11**), which includes the discussion of various combinations of initial conditions and parameter values on the motion of the structure. Polygonal trajectories, linked to polar jet streams and vortex flows, also exist at the poles of planets, influenced by the combined effects of the planet's rotation and gravity. For example, Saturn's North Pole is surrounded by a six-sided jet stream as illustrated in Fig. 8, which was initially discovered by the Voyager spacecraft in the early 1980s and later observed by Cassini [see, for example (**75**)]. An analysis of these observations is detailed in (**76**). The numerical simulations of Saturn's atmosphere, as a three-dimensional spherical layer, were provided in (**71**) to model the ripples in the jet stream flows—it is also noted that the hexagonal shape was not shown in the simulations presented in the paper, but formation of ripples is clearly visible in the computational plots. Here, we demonstrate that the formation of the approximate polygonal shape is governed by two simple mechanisms: gyroscopic effects and gravity. Eight cyclonic vortices appear around a central vortex at the North Pole of Jupiter, while its South Pole consists of five vortices surrounding a central vortex [see (**77**)]. An approximate pentagonal jet stream is present at the South Pole of Earth as shown in Fig. 9. The numerical analysis of the shallow water equations to investigate the stability of Mars-like annular vortices was discussed in (**78**). Laboratory models demonstrating stable polygonal patterns of vortex liquid sloshing in cylindrical containers were presented in (**72** to **74**, **81**).

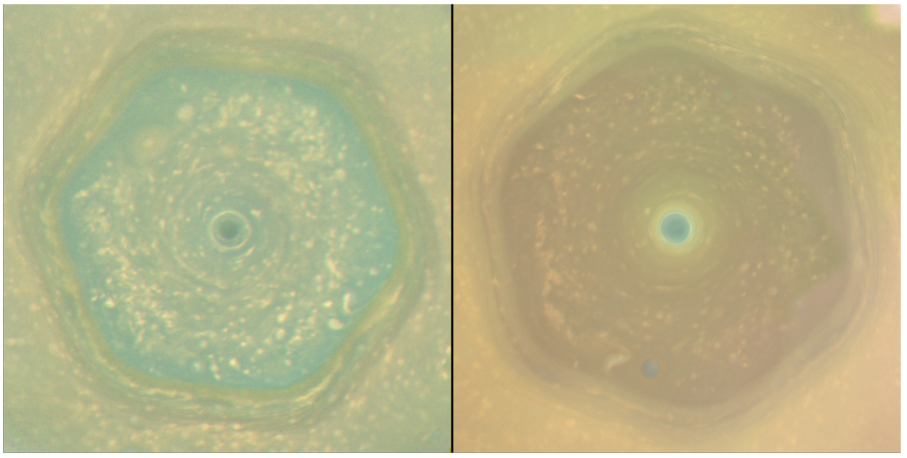

Fig. 8 Images from NASA's Cassini mission showing the appearance of Saturn's North Pole in June 2013 (left image) and April 2017 (right image), revealing the distinctive six-sided jet stream known as the 'hexagon'. Image courtesy of NASA, retrieved from https://www.jpl.nasa.gov/images/pia21611-saturns-hexagon-as-summer-solstice-approaches as of March 2025

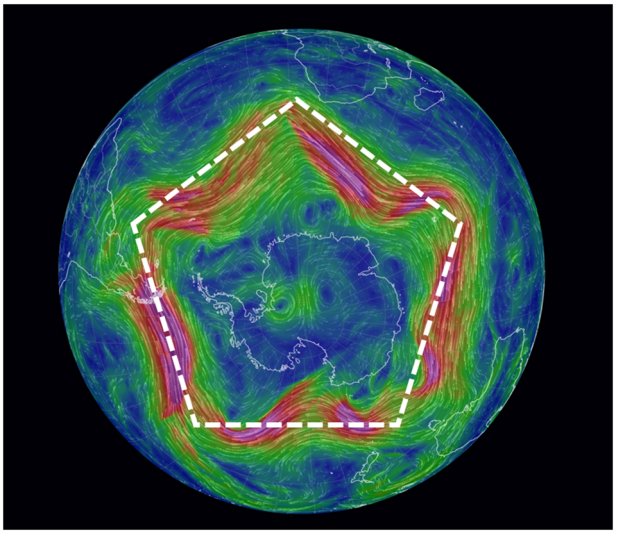

Fig. 9 Approximate pentagonal jet stream, of 3rd January 2023, at the South Pole of Earth, reproduced from https://earth.nullschool.net/#2023/01/03/1300Z/wind/isobaric/250hPa/orthographic. The approximate pentagonal shape has been highlighted

3.2. *Dimensionless system of equations*

The dimensionless system of equations of a gyropendulum are expressed as follows (**11**, **23**, **82**)

$$\frac{d^2}{d\tilde{t}^2}\begin{pmatrix}\tilde{u}\\ \tilde{v}\end{pmatrix} + \Gamma\mathbf{R}\frac{d}{d\tilde{t}}\begin{pmatrix}\tilde{u}\\ \tilde{v}\end{pmatrix} + \begin{pmatrix}\tilde{u}\\ \tilde{v}\end{pmatrix} = \begin{pmatrix}0\\ 0\end{pmatrix}, \tag{3.5}$$

where $\tilde{t}$ is the dimensionless time variable, Γ characterises the combined effects of gravity and gyricity as well as the gyropendulum's geometry, while $\tilde{\mathcal{U}} = \tilde{\mathcal{U}}(\tilde{t})$ and $\tilde{\mathcal{V}} = \tilde{\mathcal{V}}(\tilde{t})$ represent the dimensionless transverse displacement components in the x- and y-directions, respectively. The rotation matrix $\mathbf{R}$ is given by

$$\mathbf{R} = \begin{pmatrix} 0 & 1 \\ -1 & 0 \end{pmatrix}. \tag{3.6}$$

(The dimensionless equations for the transverse displacement components of the gyropendulum can also be obtained by introducing the dimensionless time $\tilde{t} = t\sqrt{g/L}$ into the system (3.4), where $\Gamma = 2\Omega\sqrt{L/g}$, $\tilde{\mathcal{U}}(\tilde{t}) = \mathcal{U}(\tilde{t}\sqrt{L/g})$ and $\tilde{\mathcal{V}}(\tilde{t}) = \mathcal{V}(\tilde{t}\sqrt{L/g})$.)
The general solution of (3.5) can be written as a linear combination of the normal mode solutions for each case of the parameter Γ. We set the initial conditions

$$\tilde{\mathcal{U}}(0) = \tilde{\mathcal{U}}_0, \;\; \tilde{\mathcal{V}}(0) = \tilde{\mathcal{V}}_0, \;\; \frac{d\tilde{\mathcal{U}}}{d\tilde{t}}(0) = \dot{\tilde{\mathcal{U}}}_0, \;\; \frac{d\tilde{\mathcal{V}}}{d\tilde{t}}(0) = \dot{\tilde{\mathcal{V}}}_0, \tag{3.7}$$

where $\tilde{\mathcal{U}}_0, \tilde{\mathcal{V}}_0, \dot{\tilde{\mathcal{U}}}_0$ and $\dot{\tilde{\mathcal{V}}}_0$ are given values of the normalised initial displacements and initial velocities. Assuming solutions of the form $\tilde{\mathcal{U}} = \mathcal{a}\exp(i\tilde{\omega}\tilde{t})$, $\tilde{\mathcal{V}} = \mathcal{b}\exp(i\tilde{\omega}\tilde{t})$, where $\mathcal{a}$ and $\mathcal{b}$ are arbitrary constants, and substituting into the system (3.5), yields the solutions of (3.5), satisfying the initial conditions (3.7), of the form

$$\begin{aligned} \begin{pmatrix} \tilde{\mathcal{U}} \\ \tilde{\mathcal{V}} \end{pmatrix} = {} & \frac{-\dot{\tilde{\mathcal{V}}}_0 + \tilde{\omega}_2\tilde{\mathcal{U}}_0}{\tilde{\omega}_1 + \tilde{\omega}_2} \begin{pmatrix} \cos(\tilde{\omega}_1\tilde{t}) \\ -\sin(\tilde{\omega}_1\tilde{t}) \end{pmatrix} + \frac{\dot{\tilde{\mathcal{U}}}_0 + \tilde{\omega}_2\tilde{\mathcal{V}}_0}{\tilde{\omega}_1 + \tilde{\omega}_2} \begin{pmatrix} \sin(\tilde{\omega}_1\tilde{t}) \\ \cos(\tilde{\omega}_1\tilde{t}) \end{pmatrix} \\ & + \frac{\dot{\tilde{\mathcal{V}}}_0 + \tilde{\omega}_1\tilde{\mathcal{U}}_0}{\tilde{\omega}_1 + \tilde{\omega}_2} \begin{pmatrix} \cos(\tilde{\omega}_2\tilde{t}) \\ \sin(\tilde{\omega}_2\tilde{t}) \end{pmatrix} + \frac{-\dot{\tilde{\mathcal{U}}}_0 + \tilde{\omega}_1\tilde{\mathcal{V}}_0}{\tilde{\omega}_1 + \tilde{\omega}_2} \begin{pmatrix} -\sin(\tilde{\omega}_2\tilde{t}) \\ \cos(\tilde{\omega}_2\tilde{t}) \end{pmatrix}, \end{aligned} \tag{3.8}$$

where

$$\tilde{\omega}_1 = \frac{1}{2}\left(-\Gamma + \sqrt{\Gamma^2 + 4}\right), \;\; \tilde{\omega}_2 = \frac{1}{2}\left(\Gamma + \sqrt{\Gamma^2 + 4}\right). \tag{3.9}$$

The analysis presented in (**82**, **83**) shows that the transverse displacements of a gyropendulum can be modelled by the trajectory of a fixed point on the circumference of a circle as the circle rolls along another fixed circle without slipping. A discussion into the formation of polygonal shapes in the trajectory of a gyropendulum, resulting from perturbations of the fundamental circular motion, is provided in (**11**, **23**, **83**). In the subsequent section, we present examples of approximate polygonal trajectories of the gyropendulum.

3.3. *Approximate polygonal trajectories*

The solutions (3.8) can be written in the complex form (**11**)

$$z(\tilde{t}) = c_1 e^{-i\tilde{\omega}_1\tilde{t}} + c_2 e^{i\tilde{\omega}_2\tilde{t}}, \tag{3.10}$$

where $z(\tilde{t}) = \tilde{\mathcal{U}}(\tilde{t}) + i\tilde{\mathcal{V}}(\tilde{t})$ and c_j, for $j = 1, 2$, are complex constants. As discussed in (**11**), when $\tilde{\omega}_2$ is chosen as an integer multiple of $\tilde{\omega}_1$, polygonal trajectories of the gyropendulum can be obtained. In

particular, requiring that the ratio $\tilde{\omega}_2/\tilde{\omega}_1 = n-1$, where $n \geq 3$ is the number of sides of the polygon, results in a gyropendulum motion approximating a regular n-sided polygon for the appropriately chosen initial conditions. This yields the following value of the quantity Γ associated with the approximate polygonal trajectory:

$$\Gamma_n = \frac{n-2}{\sqrt{n-1}}. \tag{3.11}$$

We also note that approximate polygonal trajectories of the gyropendulum can be obtained for $\Gamma < 0$ with the appropriate initial conditions. However, here we consider the case of $\Gamma > 0$. In this case, the initial conditions at the end of the gyropendulum are chosen as [see (**11**)]

$$\tilde{\mathcal{U}}_0 = \mathcal{R},\ \tilde{\mathcal{V}}_0 = 0,\ \dot{\tilde{\mathcal{U}}}_0 = 0,\ \dot{\tilde{\mathcal{V}}}_0 = \frac{\mathcal{R}(2-n)\sqrt{n-1}}{2+n(n-1)}, \tag{3.12}$$

where $\mathcal{R}$ is linked to the size of the approximate polygon.

The non-dimensional transverse displacements of the gyropendulum, satisfying the initial conditions (3.12) and approximating an n-sided regular polygon, are then given by

$$\begin{pmatrix}\tilde{\mathcal{U}}_n\\ \tilde{\mathcal{V}}_n\end{pmatrix} = \frac{\mathcal{R}n(n-1)}{n^2-n+2}\begin{pmatrix}\cos\left(\frac{\tilde{t}}{\sqrt{n-1}}\right)\\ -\sin\left(\frac{\tilde{t}}{\sqrt{n-1}}\right)\end{pmatrix} + \frac{2\mathcal{R}}{n^2-n+2}\begin{pmatrix}\cos(\tilde{t}\sqrt{n-1})\\ \sin(\tilde{t}\sqrt{n-1})\end{pmatrix}.$$

In Fig. 10(a) and (b), we present the approximating polygonal trajectories of the gyropendulum with $\mathcal{R} = 0.01$ for a pentagonal and hexagonal shape, respectively. For the example in Fig. 10(a), $n = 5$ which results in $\tilde{\omega}_1 = 1/2, \tilde{\omega}_2 = 2$ and $\Gamma_5 = 3/2$. In this case, the transverse displacements are given by

$$\begin{pmatrix}\tilde{\mathcal{U}}_5\\ \tilde{\mathcal{V}}_5\end{pmatrix} = \frac{1}{110}\begin{pmatrix}\cos(\frac{\tilde{t}}{2})\\ -\sin(\frac{\tilde{t}}{2})\end{pmatrix} + \frac{1}{1100}\begin{pmatrix}\cos(2\tilde{t})\\ \sin(2\tilde{t})\end{pmatrix}, \tag{3.13}$$

and the trajectory is periodic with the period 4π. The transverse displacements in Fig. 10(b) are associated with $n = 6$, resulting in $\tilde{\omega}_1 = \sqrt{5}/5, \tilde{\omega}_2 = \sqrt{5}$ and $\Gamma_6 = 4\sqrt{5}/5$, and are given by

$$\begin{pmatrix}\tilde{\mathcal{U}}_6\\ \tilde{\mathcal{V}}_6\end{pmatrix} = \frac{3}{320}\begin{pmatrix}\cos(\frac{\tilde{t}\sqrt{5}}{5})\\ -\sin(\frac{\tilde{t}\sqrt{5}}{5})\end{pmatrix} + \frac{1}{1600}\begin{pmatrix}\cos(\tilde{t}\sqrt{5})\\ \sin(\tilde{t}\sqrt{5})\end{pmatrix}. \tag{3.14}$$

Hence, the period of the approximating hexagonal trajectory is given by $2\pi\sqrt{5}$. It is noted that the change in the polygonal trace of the gyropendulum from the pentagonal to the hexagonal trajectory is associated with a change in the parameter Γ and a different prescribed initial velocity in the y-direction. The same method applies for approximating polygonal shapes of a higher-order symmetry,

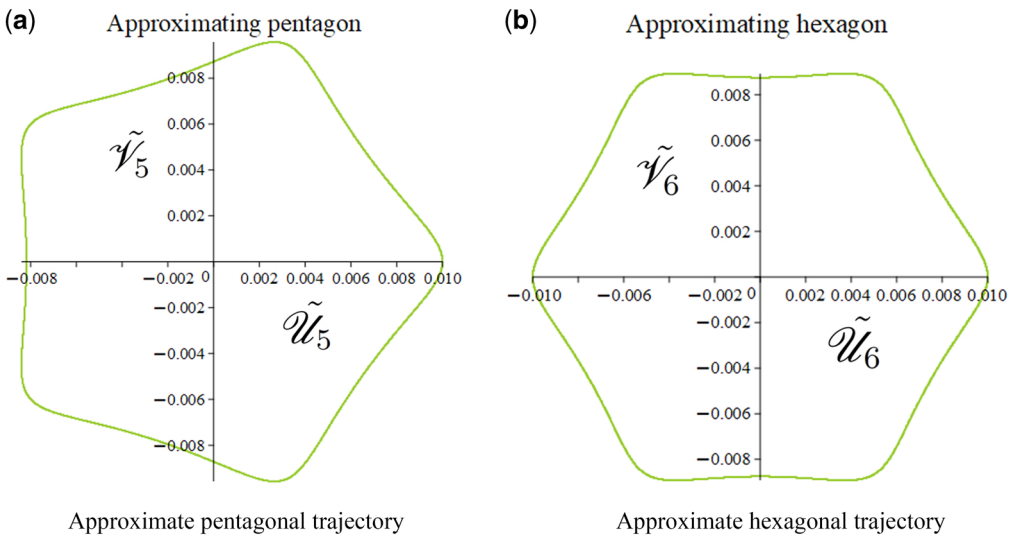

Fig. 10 The polygonal approximate trajectories of the gyropendulum. (a) The pentagon approximation with $n = 5$, $\Gamma_5 = 3/2$, $\tilde{u}_0 = 0.01$, $\tilde{v}_0 = 0$, $\dot{\tilde{u}}_0 = 0$ and $\dot{\tilde{v}}_0 = -0.0027$, and (b) the hexagon approximation with $n = 6$, $\Gamma_6 = 4\sqrt{5}/5$, $\tilde{u}_0 = 0.01$, $\tilde{v}_0 = 0$, $\dot{\tilde{u}}_0 = 0$ and $\dot{\tilde{v}}_0 = -0.0028$.

where the segments do not have to be linear. Moreover, we also note that the polygonal trajectories of the gyropendulum can be obtained for different orientations of the spinner's rotation. The analysis presented in this section demonstrates how the gyropendulum's polygonal motions change with different parameters and initial conditions [see also (**11**, **23**)], providing an approximate comparison with the polygonal formations observed at the poles of rotating planets.

4. Concluding remarks

In this paper we have presented an analytical approach to modelling the shallow water equations in equatorial regions, as well as polar regions. In the first case, the asymptotic method is fully consistent with the boundary conditions on the sides of the equatorial band, which allows for a description of the meridionally bounded propagating waves. The results of the theory presented in this series of two papers provide a connection between equatorial waves in a continuum and chiral gravitational waves in a discrete structure, with the primary focus on the combined characteristics of chirality and gravity in both models.

In the discrete models, studied in part 1 of the paper, chiral gravitational waves possess unique directional propagating properties due to their physical chirality through the presence of spinners, as well as the influence of gravity. These characteristics allowed for the description of eastward- and westward-moving elastic vortex waves along the discrete lattice strip as discussed in part 1. Conversely, equatorial atmospheric phenomena occur due to the complex inertial and rotational dynamics in the vicinity of the equator. In equatorial regions, atmospheric and oceanic dynamics exhibit unique behaviours driven by the interactions between solar heating, the Earth's rotation, gravitational forces and atmospheric circulation patterns. These phenomena give rise to processes

such as equatorial waves, the Intertropical Convergence Zone (ITCZ) (**84**) and the El Niño-Southern Oscillation (ENSO) (**85**, **86**).

For the description of polar vortices, the motion of a single gyropendulum has also been discussed in connection with the approximate planar flow of a fluid ridge. Polygonal pattern formations of the gyropendulum are presented, which are also observed on the poles of rotating planets, where the gravitational and gyroscopic dynamics can result in different types of fluid motions. For a gyropendulum, controlling the gyricity through the spinner or the gravitational action leads to changes in its motion, formally providing an approximate analogy to the distinct characteristics observed in fluid flows.

The novel modelling of waves presented in this paper for various domains provides fundamental insights into wave dynamics influenced by rotational and gravitational forces. The methods and results of this paper are directly applicable to analysing the mechanisms governing atmospheric and oceanic flows.

Author contributions

All the authors of the article, A.K., I.S.J., N.V.M, A.B.M., have contributed to the conception of the work, analysis, interpretation of data, and writing the text of the article.

Acknowledgments

A. Kandiah gratefully acknowledges the financial support of the EPSRC through the Mathematics DTP grant EP/V52007X/1, project reference 2599756.

Data availability

All analytical data analysed during this study are included in this published paper.

Conflict of Interest

All authors declare that there is no conflict of interest.

References

1. D. Andrews, J. Holton and C. Leovy, *Middle Atmosphere Dynamics*. (Academic press, Orlando, USA 1987).
2. J. Pedlosky, *Geophysical Fluid Dynamics*. (Springer Science & Business Media, New York, USA 2013).
3. J. Boyd, *Dynamics of the Equatorial Ocean*. (Springer, Berlin, Germany 2018).
4. D. Moore, *Planetary-Gravity Waves in an Equatorial Ocean*. (Harvard University, Cambridge, USA 1968).
5. A. Gill, *Atmosphere-Ocean Dynamics*. (Academic Press, New York, USA 1982).
6. M. Takahashi, Simulation of the stratospheric quasi-biennial oscillation using a general circulation model, *Geophys. Res. Lett*. **23** (1996) 661–664.
7. M. Takahashi and B. Boville, A three-dimensional simulation of the equatorial quasi-biennial oscillation, *J. Atmos. Sci.* **49** (1992) 1020–1035.
8. M. Wheeler, G. Kiladis and P. Webster, Large-scale dynamical fields associated with convectively coupled equatorial waves, *J. Atmos. Sci.* **57** (2000) 613–640.

9. C. Menkes, J. Vialard, S. Kennan, J. Boulanger and G. Madec, A modeling study of the impact of tropical instability waves on the heat budget of the Eastern Equatorial Pacific, *J. Phys. Oceanogr*. **36** (2006) 847–865.

10. G. Yang, S. Ferrett, S. Woolnough, J. Methven and C. Holloway, Real-time identification of equatorial waves and evaluation of waves in global forecasts, *Weather Forecast* **36** (2021) 171–193.

11. A. Kandiah, I. S. Jones, N. V. Movchan, A. B. Movchan. *et al*, Effect of gravity on the dispersion and wave localisation in gyroscopic elastic systems, *Mechanics of Heterogeneous Materials. Advanced Structured Materials*, Vol. **195** (ed. H. Altenbach; Springer, Cham, Switzerland 2023) 219–274.

12. I. Jones, N. Movchan and A. Movchan, Two-dimensional waves in a chiral elastic chain: dynamic green's matrices and localised defect modes, *Q. J. Mech. Appl. Math*. **73** (2021) 305–328.

13. M. Brun, I. Jones and A. Movchan, Vortex-type elastic structured media and dynamic shielding, *Proc. R Soc. A* **468** (2012) 3027–3046.

14. M. Garau, G. Carta, M. Nieves, I. Jones, N. Movchan and A. Movchan, Interfacial waveforms in chiral lattices with gyroscopic spinners, *Proc. Math. Phys. Eng. Sci.* **474** (2018) 20180132.

15. G. Carta, I. Jones, N. Movchan, A. Movchan and M. Nieves, Deflecting elastic prism" and unidirectional localisation for waves in chiral elastic systems, *Sci. Rep.* **7** (2017) 26.

16. M. Lighthill, Dynamic response of the Indian Ocean to onset of the southwest monsoon, *Philos. Trans. R. Soc. A* **265** (1969) 45–92.

17. T. Matsuno, Quasi-geostrophic motions in the equatorial area, *J. Meteorol. Soc. Japan* **44** (1966) 25–43.

18. E. Lorenz, The nature and theory of the general circulation of the atmosphere, *WMO* (1967) 161.

19. G. V. Hadley, Concerning the cause of the general trade-winds, *Philos. Trans. R. Soc*. **39** (1735) 58–62.

20. N. Paldor, *Shallow Water Waves on the Rotating Earth* (Springer, Cham, Switzerland 2015).

21. C. Erlick, N. Paldor and B. Ziv, Linear waves in a symmetric equatorial channel, *Quart. J. Royal Meteoro. Soc.* **133** (2007) 571–577.

22. W. Whitford and B. Duval, *Ecology of Desert Systems* (Academic Press, San Diego, USA 2019).

23. A. Kandiah, I. Jones, N. Movchan and A. Movchan, Controlling the motion of gravitational spinners and waves in chiral waveguides, *Sci. Rep.* **14** (2024) 1203.

24. G Veronis, On the transient response of a β-plane ocean, *J. Oceanogr. Soc. Japan* **14** (1958) 1–5.

25. G. Veronis. On the approximations involved in transforming the equations of motion from a spherical surface to the β-plane. I. *Barotropic Systems, J. Mar. Res*. 21 (1963) 110–124.

26. G. Veronis. On the approximations involved in transforming the equations of motion from a spherical surface to the β-plane. II. *Baroclinic Systems, J. Mar. Res*. 21 (1963) 199–204.

27. M. Stern, Trapping of low frequency oscillations in an equatorial "boundary layer", *Tellus* **15** (1963) 246–250.

28. F. Bretherton, Low frequency oscillations trapped near the equator, *Tellus* **16** (1964) 181–185.

29. G. Kiladis, M. Wheeler, P. Haertel, K. Straub and P. Roundy, Convectively coupled equatorial waves, *Rev. Geophys*. **47** (2009), RG2003, 42 pages.

30. R. Blandford, Mixed gravity-Rossby waves in the ocean, *Deep Sea Res*. **13** (1966) 941–961.

31. P. Delplace, J. Marston and A. Venaille, Topological origin of equatorial waves, *Science* **358** (2017) 1075–1077.

32. M. Marciani and P. Delplace, Chiral maxwell waves in continuous media from Berry monopoles, *Phys. Rev. A*. **101** (2020) 023827.
33. W. Kessler and M. McPhaden, Oceanic equatorial waves and the 1991-93 El Niño, *J. Climate* **8** (1995) 1757–1774.
34. M. McPhaden and X. Yu, Equatorial waves and the 1997-98 El niño, *Geophys. Res. Lett*. **26** (1999) 2961–2964.
35. W. Munk and D. Moore, Is the Cromwell current driven by equatorial Rossby waves?, *J. Fluid Mech.* **33** (1968) 241–259.
36. K. Straub and G. Kiladis, Observations of a convectively coupled Kelvin wave in the Eastern Pacific ITCZ, *J. Atmos. Sci.* **59** (2002) 30–53.
37. Y. Takayabu, Large-scale cloud disturbances associated with equatorial waves. Part I: spectral features of the cloud disturbances, *J. Meteorol. Soc. Jpn. Ser. II* **72** (1994) 433–449.
38. Y. Takayabu, Large-scale cloud disturbances associated with equatorial waves Part II: westward-propagating inertio-gravity waves, *J. Meteorol. Soc. Jpn. Ser. II* **72** (1994) 451–465.
39. J. Tindall, J. Thuburn and E. Highwood, Equatorial waves in the lower stratosphere. I: a novel detection method, *Q. J. R. Meteoro. Soc.* **132** (2006) 177–194.
40. G. Yang, B. Hoskins and J. Slingo, Convectively coupled equatorial waves: a new methodology for identifying wave structures in observational data, *J. Atmos. Sci.* **60** (2003) 1637–1654.
41. M. Yanai and M. Murakami, Spectrum analysis of symmetric and antisymmetric equatorial waves, *J. Meteorol. Soc. Jpn*. **48** (1970) 331–347.
42. T. Maruyama, Large-scale disturbances in the equatorial lower stratosphere, *J. Meteorol. Soc. Jpn*. **45** (1967) 391–408.
43. M. Yanai and T. Maruyama, Stratospheric wave disturbances propagating over the equatorial Pacific, *J. Meteorol. Soc. Jpn*. **44** (1966) 291–294.
44. J. Wallace and V. Kousky, Observational evidence of Kelvin waves in the tropical stratosphere, *J. Atmos. Sci.* **25** (1968) 900–907.
45. M. Cane and E. Sarachik, Forced baroclinic ocean motions. I. The linear equatorial unbounded case, *J. Mar. Res.* **34** (1976) 629–665.
46. M. Cane and E. Sarachik, Forced baroclinic ocean motions: II. The linear equatorial bounded case, *J. Mar. Res.* 35 (1977) 395–432.
47. A. Ronveaux and F. Arscott, *Heun's Differential Equations* (Clarendon Press, Oxford, UK 1995).
48. M. Abramowitz and I. Stegun, *Handbook of Mathematical Functions with Formulas, Graphs, and Mathematical Tables* (Academic Press, New York, USA 1975).
49. H. Weber, Ueber die integration der partiellen differentialgleichung, *Math. Ann.* **1** (1869) 1–36.
50. S. Philander, *El Niño, La Niña, and the Southern Oscillation* (Academic Press, San Diego 1990).
51. M. Cane and E. Sarachik, Forced baroclinic ocean motions, III: the linear equatorial basin case, *J. Mar. Res.* 37 (1979) 355–398.
52. S. Philander. The effects of coastal geometry on equatorial waves (forced waves in the Gulf of Guinea), *J. Mar. Res.* 35 (1977) 509–523.
53. B. Wang, Kelvin waves, *Encyclopedia of Meteorology,* 1062-1068, (Academic Press, New York, USA 2002).
54. C. Eriksen, M. Blumenthal, S. Hayes and P. Ripa, Wind-generated equatorial Kelvin waves observed across the Pacific Ocean, *J. Phys. Oceanogr.* **13** (1983) 1622–1640.
55. K. Saha, *The Earth's Atmosphere: Its Physics and Dynamics* (Springer, Berlin, Germany 2008).
56. R. Grove and G. Adamson, *El Niño in World History* (Palgrave Macmillan, London, UK 2018).

57. M. Moseley, Punctuated equilibrium: searching the ancient record for El Niño, *Q. Rev. Archaeol*. **8** (1987) 7–10.
58. BBC Horizon, The Lost Civilisation of Peru (2005). Programme summary. https://www.bbc.co.uk/sn/tvradio/programmes/horizon/peru_prog_summary.shtml
59. P. Rhines, Rossby waves, *Encyclopedia Of Atmospheric Sciences*, Vols. 1–6 (eds. J. R. Holton, J. A. Pyle and J. A. Curry; Elsevier, Amsterdam, Netherlands 2003) 1923–1939. https://app.knovel.com/hotlink/toc/id:kpEASV0002/encyclopedia-atmospheric/encyclopedia-atmospheric
60. H. Elbern and P. Speth, Energy of Rossby waves as a part of global atmospheric oscillations, *Tellus A Dyn. Meteorol. Oceanogr*. **45** (1993) 168–192.
61. C. Liu, X. Ren and X. Yang, Mean flow-storm track relationship and Rossby wave breaking in two types of El-Niño, *Adv. Atmos. Sci.* **31** (2014) 197–210.
62. W. Quinn, V. Neal and S. Mayolo, El Niño occurrences over the past four and a half centuries, *J. Geophys. Res. Oceans* **92** (1987) 14449–14461.
63. A. Caramanica, L. Huaman Mesia, C. Morales, G. Huckleberry, L. Castillo B and J. Quilter, El Niño resilience farming on the North Coast of Peru, *Proc. Natl. Acad. Sci. USA* **117** (2020) 24127–24137.
64. M. Moseley, R. Feldman, C. Ortloff and A. Narvaez, Principles of agrarian collapse in the Cordillera Negra, Peru, *Ann. Carnegie Mus*. **52** (1983) 299–327.
65. M. Moseley and J. Richardson, Doomed by natural disaster, *Archaeology* **45** (1992) 44–45.
66. I. S. Gradshteyn and I. M. Ryzhik, *Table of Integrals, Series, and Products*, 6th edn. (Academic Press, San Diego 2000).
67. E. Whittaker and G. Watson, *A Course of Modern Analysis: An Introduction to the General Theory of Infinite Processes and of Analytic Functions; with an account of the Principal Transcendental Functions* (Cambridge University Press, Cambridge, UK 1920).
68. D. Chart, *A Study of Coastally Trapped, Intraseasonal Waves of Equatorial Origin in the Global Oceans Using TOPEX/POSEIDON Altimeter Data* (University of Colorado at Boulder, Boulder, USA 1998).
69. P. LeBlond and L. Mysak, *Waves in the Ocean* (Elsevier, New York, USA 1978).
70. J. Siliezar. Interplanetary storm chasing. *The Harvard Gazette* (2020). https://news.harvard.edu/gazette/story/2020/10/3d-model-seeks-to-explain-mysterious-hexagon-storm-on-saturn/
71. R. Yadav and J. Bloxham, Deep rotating convection generates the polar hexagon on Saturn, *Proc. Natl. Acad. Sci. USA* **117** (2020) 13991–13996.
72. G. Vatistas, A note on liquid vortex sloshing and Kelvin's equilibria, *J. Fluid Mech.* **217** (1990) 241–248. p
73. T. Jansson, M. Haspang, K. Jensen, P. Hersen and T. Bohr, Polygons on a rotating fluid surface, *Phys. Rev. Lett*. **96** (2006) 174502.
74. Á. Kadlecsik, Á. Szeidemann and M. Vincze, A simple approximation for the drift rates of rotating polygons on a free fluid surface, *Eur. Phys. J. Spec. Top.* **232** (2023) 453–459.
75. A. Ingersoll, Cassini exploration of the planet Saturn: a comprehensive review, *Space Sci. Rev.* **216** (2020) 122.
76. M. Allison, D. Godfrey and R. Beebe, A wave dynamical interpretation of Saturn's polar hexagon, *Science* **247** (1990) 1061–1063.
77. F. Tabataba-Vakili, J. Rogers, G. Eichstädt, G. Orton, C. Hansen, T. Momary, J. Sinclair, R. Giles, M. Caplinger, M. Ravine and S. Bolton, Long-term tracking of circumpolar cyclones on Jupiter from polar observations with JunoCam, *Icarus* **335** (2020) 113405.

78. W. Seviour, D. Waugh and R. Scott, The stability of Mars's annular polar vortex, *J. Atmos. Sci*. **74** (2017) 1533–1547.
79. O. Kirillov and M. Levi, Rotating saddle trap as Foucault's pendulum, *Am. J. Phys*. **84** (2016) 26–31.
80. O. Kirillov, *Non-Conservative Stability Problems of Modern Physics* (Walter de Gruyter GmbH & Co KG, Berlin, Germany 2021).
81. A. Aguiar, P. Read, R. Wordsworth, T. Salter and Y. Yamazaki, A laboratory model of Saturn's North polar hexagon, *Icarus* **206** (2010) 755–763.
82. A. Kandiah *et al* (2024). Interaction between gravity and gyroscopic forces: transient control of gyropendulums and inverted gyropendulums. *Proceedings of 14th International Symposium on Continuum Models and Discrete Systems (CMDS14)*, 26–30 June 2023, Paris. Springer collection *Proceedings in Mathematics and Statistics*.
83. I. Kandiah, A. Movchan, N. Movchan and A. Jones, In a spin over gravity, *Mathematics Today* **60** (2024) 79–84.
84. T. Schneider, T. Bischoff and G. Haug, Migrations and dynamics of the intertropical convergence zone, *Nature* **513** (2014) 45–53.
85. E. Rasmusson and J. Wallace, Meteorological aspects of the El Niño/Southern oscillation, *Science* **222** (1983) 1195–1202.
86. Y. Wang, A. Gozolchiani, Y. Ashkenazy and S. Havlin, Oceanic El-Niño wave dynamics and climate networks, *New J. Phys.* **18** (2016) 033021.
87. J. Holton and R. Lindzen, A note on "Kelvin" waves in the atmosphere, *Mon. Weather Rev*. **96** (1968) 385–386.
88. C. Eckart, The propagation of gravity waves from deep to shallow water. *Proceedings Of NBS Semicentennial Symposium on Gravity Waves Held at the NBS On June 18–20, 1951*. Vol. 521(National Bureau of Standards, Washington D.C., USA 1952) 165–173.
89. C. Rossby, Collaborators, Relation between variations in the intensity of the zonal circulation of the atmosphere and the displacements of the semi-permanent centers of action, *J. Mar. Res.* **2** (1939) 38–55.
90. J. Snyder, *Map projections-A Working Manual* (US Government Printing Office, Washington D.C., USA 1987).
91. R. Rapp, The equatorial radius of the Earth and the zero-order undulation of the geoid, *J. Geophys. Res.* **72** (1967) 589–593.
92. D. Frierson, J. Lu and G. Chen, Width of the Hadley cell in simple and comprehensive general circulation models, *Geophys. Res. Lett*. **34** (2007) L18804.
93. Y. Daoxian, Variations of Karst Geomorphology over Geoclimatic Gradients, *Treatise of Geomorphology* **6** (2013) 319–326.
94. M. Wheeler and G. Kiladis, Convectively coupled equatorial waves: analysis of clouds and temperature in the wavenumber-frequency domain, *J. Atmos. Sci.* **56** (1999) 374–399.
95. W. Magnus, F. Oberhettinger and R. P. Soni, *Formulas and theorems for the special functions of mathematical physics*. 3rd enlarged edn (Springer, Berlin, Heidelberg 1966), Available at: https://doi.org/10.1007/978-3-662-11761-3
96. L. Slater, *Confluent Hypergeometric Functions* (Cambridge University Press, London and New York 1960).
97. G. Watson, *A Treatise on the Theory of Bessel Functions* (Cambridge University Press, Cambridge, UK 1922).

Appendix A. Kelvin waves

In this section we analyse the non-dispersive Kelvin waves, which are a type of equatorial waves that occur in rotating fluid systems. Kelvin waves propagate parallel to the equator or coastlines (**50**, **87**), with no meridional velocity variations, and thus we take $v(x,y,t)=0$ (see Section 2). In the description of Kelvin waves, the conditions at the boundaries of the equatorial band are important since the wave amplitudes can increase away from the boundaries. Such waves can also propagate along interfaces between regions of different fluid densities. Then, setting $v=0$ in the equations (1.1) and (1.3) of the main text, and eliminating one of the variables yields the following dispersion relation:

$$\omega^2 = gHk^2. \tag{A.1}$$

The above dispersion equation for Kelvin waves also represents the shallow water gravity waves dispersion relation [see, for example (**88**)]. By taking into account (A.1), we write the phase speed of the Kelvin waves in the zonal x-direction, as follows:

$$c = \frac{\omega}{k} = \pm\sqrt{gH}. \tag{A.2}$$

The quantity (A.2) refers to the velocity at which the phase of the waves propagates in the spatial direction. Additionally, the group velocities of the Kelvin waves, which represent the velocities of the oscillating wave packets in the medium, are given by $\pm\sqrt{gH}$. The eastward-propagating waves are known as the Kelvin waves, while the westward-propagating waves are referred to in the literature as the anti-Kelvin waves [see, for example (**50**, **51**)]. They are distinguished by their amplitudes away from the equator as well as their direction of propagation.

By combining equations (1.1) and (1.3) of Section 1 with the additional condition that $v=0$, we obtain the following wave equations:

$$\frac{\partial^2 u}{\partial t^2} = gH\frac{\partial^2 u}{\partial x^2}, \quad \frac{\partial^2 h}{\partial t^2} = gH\frac{\partial^2 h}{\partial x^2}. \tag{A.3}$$

Thus, the time-harmonic variations of u and h in the domain (x,t) are given by $e^{ik(x+ct)}$. Finally, (1.2) in the main text is used to determine the y-dependence for the quantities u and h, yielding the time-harmonic representations for the zonal and meridional velocities and height field, respectively, as follows

$$u = \mathrm{Re}\Big\{ -\frac{g}{c}h_0 e^{-\frac{2\Omega R}{c}\cos(\frac{y}{R})}e^{ik(x+ct)}\Big\}, \quad v=0, \quad h = \mathrm{Re}\Big\{h_0 e^{-\frac{2\Omega R}{c}\cos(\frac{y}{R})}e^{ik(x+ct)}\Big\}, \tag{A.4}$$

where h_0 is an arbitrary constant. The sign of c [see (A.2)] determines the direction of propagation for the travelling Kelvin waves. For $\Omega>0$, if $c>0$, the amplitude of the waveform decreases as y increases, whereas if $c<0$, the wave amplitude increases as y increases.

Applying the normalisations (2.9) of Section 2.1 together with $x=R\tilde{X}$ and $t=\sqrt{R/g}\tilde{T}$, where the quantities with the symbol '$\sim$' are dimensionless, to the dimensional representations (A.4), yields the following non-dimensional forms for the zonal and meridional velocities and height field of the Kelvin modes (the symbol '$\sim$' has been dropped for convenience)

$$\begin{aligned} \hat{u} &= -\frac{h_0}{\hat{c}}e^{-\frac{\Omega}{\hat{c}}\cos(Y)}\cos(k(X+\hat{c}T)), \\ \hat{v} &= 0, \\ \hat{h} &= h_0 e^{-\frac{\Omega}{\hat{c}}\cos(Y)}\cos(k(X+\hat{c}T)), \end{aligned} \tag{A.5}$$

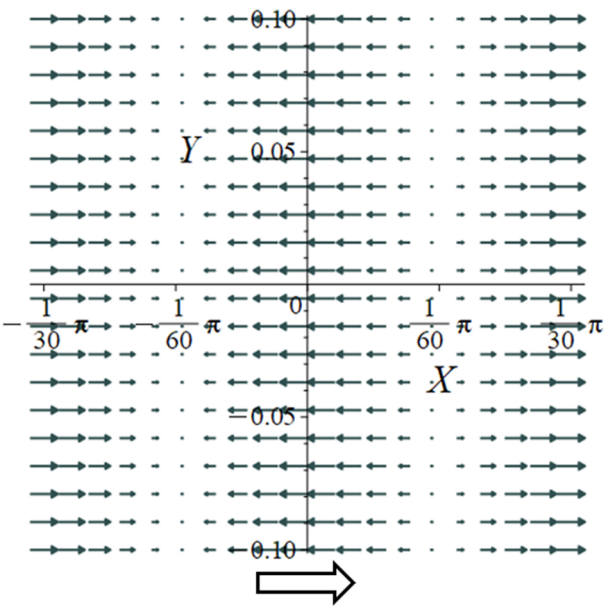

Fig. A1 Eastward-propagating Kelvin mode for $(k,\omega) = (30, 6.7082)$ with the velocity components defined by (A.5), for $h_0 = 1$ and the dimensionless parameter values $\Omega = 0.25$, $H = 0.05$ and $\epsilon = 0.1$. The non-dimensional propagation speed is $\hat{c} = 0.2236$.

where $\hat{u}(X,Y,T) = \sqrt{\frac{R}{g}}u\left(RX, RY, \sqrt{\frac{R}{g}}T\right), \hat{v}(X,Y,T) = \sqrt{\frac{R}{g}}v\left(RX, RY, \sqrt{\frac{R}{g}}T\right), \hat{h}(X,Y,T) = h\left(RX, RY, \sqrt{\frac{R}{g}}T\right)$ and the normalised velocity is given by $\hat{c} = \pm\sqrt{H}$ for the Kelvin and anti-Kelvin waves, respectively. The non-dimensional dispersion relation for the non-dispersive Kelvin waves is

$$\omega = \hat{c}k. \tag{A.6}$$

Thus, the normalised phase speeds and group velocities of the Kelvin waves are given by $\pm\sqrt{H}$.

A typical example of an eastward-propagating Kelvin wave is shown in Fig. A1, where the zonal velocities are non-zero and the meridional velocities vanish, for the parameter values $H = 0.05, \Omega = 0.25$ and $\epsilon = 0.1$. The non-dimensional eigenfunctions of the Kelvin mode displayed in Fig. A1 are defined by (A.5) with $h_0 = 1$. These waves are non-dispersive and propagate either eastward or westward along the narrow equatorial band, depending on the sign of the group velocity. We note that the phase and group velocities of the Kelvin waves are either both positive or both negative. Compared to Rossby and inertia-gravity waves discussed in the main text of the paper, Kelvin waves typically do not exhibit standing modes. Moreover, Kelvin waves do not display vortices, unlike Rossby modes, and are characterised by their horizontal motion as shown in Fig. A1. As discussed in the main text, Kelvin, Rossby and inertia-gravity waves show distinct dispersion and propagation properties, resulting in different spatial and temporal patterns of the equatorial fluid motions.

Appendix B. Comparison of the dispersion properties between the harmonic wave model and the Matsuno model

In this section, we present a quantitative comparison between the dispersion properties of the trapped equatorial waves found in Matsuno (**17**) and the dispersion relation of the harmonic waves derived in Section 2.3 of the main text. The equatorial channel solution derived by Matsuno considered wave motions in an unbounded plane and neglected the $O((y/R)^3)$ term in the expansion of $\sin(y/R)$, which is essential in the derivation of the meridional velocity equation (see Section 2.1). The analysis presented here addresses the equatorial channel problem formulation with Dirichlet boundary conditions, and introduces a novel asymptotic perturbation method to examine the eigenfunctions and eigenvalues.

We consider the meridional velocity mode in a narrow equatorial band, reduced to the dimensional form of the harmonic oscillator equation (see Section 2):

$$\frac{d^2B}{dy^2}+\Big[\frac{\omega^2}{gH}-k^2+\frac{k\beta}{\omega}\Big]B(y)=0,\quad B(\pm a)=0, \tag{B.1}$$

where $\beta=2\Omega/R$ is the Rossby parameter (**89**), and the remaining variables and parameters are defined in Sections 1 and 2.1. Introducing the dimensionless variables

$$\tilde{Y}=\frac{y}{R},\quad \tilde{\omega}=\frac{\omega}{\sqrt{\beta\sqrt{gH}}},\quad \tilde{k}=k\sqrt{\frac{\sqrt{gH}}{\beta}}, \tag{B.2}$$

where the quantities with the symbol '$\sim$' are dimensionless, the eigenvalue problem (B.1) can be re-written as follows (where the '$\sim$' has been dropped for convenience):

$$\frac{d^2\hat{B}}{dY^2}+\frac{R^2\beta}{\sqrt{gH}}\Big[\omega^2-k^2+\frac{k}{\omega}\Big]\hat{B}(Y)=0,\quad \hat{B}(\pm a/R)=0, \tag{B.3}$$

where $\hat{B}(Y)=B(RY)$. Following a similar analysis to that in Section 2.3, and assuming the condition

$$\omega^2-k^2+\frac{k}{\omega}>0, \tag{B.4}$$

which applies for non-trivial and bounded solutions of the eigenvalue problem (B.3), the following non-dimensional dispersion equation can be deduced from the above problem:

$$\omega^2-k^2+\frac{k}{\omega}=\Upsilon j^2,\quad j=1,2,3,\ldots, \tag{B.5}$$

where $\Upsilon=\frac{\pi^2}{4a^2}\frac{\sqrt{gH}}{\beta}$, which is dependent on the depth H and strip width $2a$. Accounting for the RHS of the above equation and the j-th equatorial mode, (B.5) is similar to Matsuno's equation (8) [see (**17**)], which is given by

$$\omega^2-k^2+\frac{k}{\omega}=2n+1,\quad n=0,1,2,\ldots, \tag{B.6}$$

where n is the meridional mode number [see also (**8**)]. We note that the special mode corresponding to $n=0$ is not captured by the dispersion relation (B.5). This mode corresponds to the mixed-Rossby gravity wave,

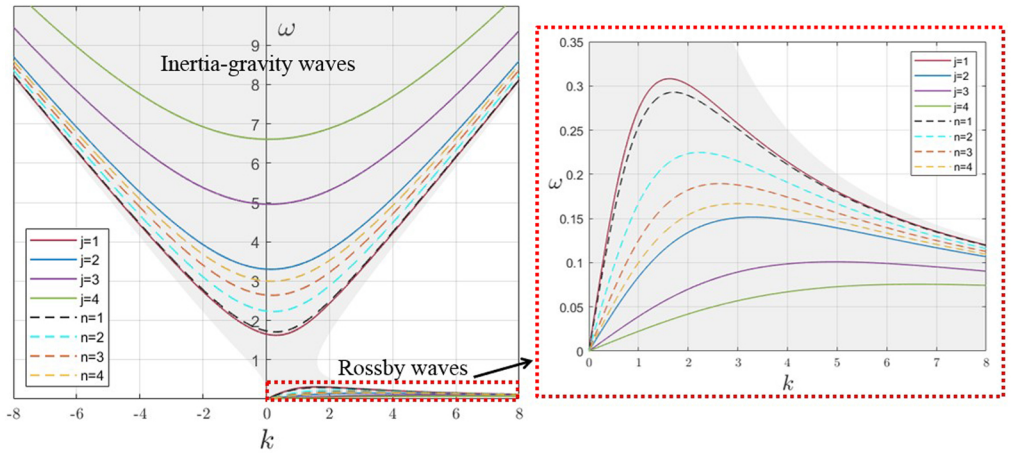

Fig. B1 Dispersion curves of the harmonic (solid) and Matsuno (dashed) models for a range of values of the meridional mode numbers. The Matsuno modes are defined by (B.6), while the harmonic modes correspond to (B.5) with $\Upsilon = 2.7274$. The shaded region corresponds to (B.4)

and it approximates an inertia-gravity wave at high frequencies and a Rossby wave at low frequencies [see, for example (**8**, **17**, **50**, **69**)]. The $n = 0$ mode is related to the infinite plane approximation used by Matsuno, and its accuracy compared to the narrow channel solution is discussed in (**20**).

Taking into account the approximation of the shape of the Earth, we set the Earth's equatorial radius of $R = 6378 \times 10^3$ m [see, for example (**90**, **91**)]. The angular speed of the Earth in inertial space can be approximated by $\Omega = 7.2921159 \times 10^{-5}$ rad/s. Then, noting that the Hadley cells extend from the equator to about 30° S in the Southern Hemisphere and 30° N in the Northern Hemisphere (**92**), and that they feature air rising near the equator, typical within 5° S to 5° N, where the Intertropical Convergence Zone is located [see (**93**)], we can approximate the latitude of the channel boundaries between 5° N to 30° N in the Northern Hemisphere and 30° S to 5° S in the Southern Hemisphere. Thus, we approximate the width parameter a [m] as follows

$$\frac{531500\pi}{3} \ (\approx 556585) < a < 1063\pi \times 10^3 \ (\approx 3339513), \tag{B.7}$$

where the approximate sphericity of the Earth is assumed.

In Fig. B1 we provide the diagram of the dispersion curves obtained by the model of Section 2.3 and the Matsuno model for positive integer values of the meridional mode numbers, which are defined by (B.5) and (B.6), respectively. The shaded region corresponding to (B.4) is shown in Fig. B1, which contains the inertia-gravity modes and the Rossby modes. Experimental analysis, involving measurements of frequencies and wavenumbers, is extremely challenging in the context of acquisition of data, but nevertheless it was possible, and the paper (**94**) provides the spectral analysis based on the satellite database accumulated over the duration of 18 years. It is not surprising that there was no uniform match with the Matsuno model, but certain dispersion curves could be mapped on the spectral peaks for a specific range of the depth values. In (**94**), the values of depth were chosen between 12 m and 200 m. In our illustrative simulation, presented in Fig. B1, we use the value $H = 100$ m approximately in the middle of that range, which is also consistent with the constraints of a barotropic model and the linearised shallow water equations. Moreover, we assume that the channel boundaries

are at 10° S and 10° N, which gives the approximate value $a = 1113171$ [m], and thus $\Upsilon = 2.7274$. This results in the solid dispersion curves of the harmonic model shown in Fig. B1, which are defined by (B.5). The dispersion curves of the inertia-gravity wave and the Rossby wave of the harmonic model corresponding to the first mode ($j = 1$) show a very good agreement with the Matsuno dispersion curves for the $n = 1$ mode as illustrated in Fig. B1. It is also noted that the lower bound for the ratio of the minimum frequency of the inertia-gravity mode to the maximum frequency of the Rossby mode for the harmonic and Matsuno models are 5.265 and 5.828, respectively, which occur at the first meridional mode. Although, this ratio increases for higher modes in both models, it will always be larger in the harmonic model than the Matsuno model for sufficiently large meridional mode numbers, which represents a significant difference between the two models. We also emphasise on the difference in approach of Section 2.3, dealing with the spectral problem in a strip, and the Matsuno model, addressing equations with unbounded coefficients in a plane.

Appendix C. Dispersion properties of the meridional velocity modes

The eigenvalue problem (2.21) of the main text represents an equatorial wave problem for the meridional velocity component, and its solutions consist of a linear combination of parabolic cylinder functions as detailed in Section 2.5, with the asymptotic approximations provided in Section 2.6. The application of the boundary conditions at $Y = \pm\epsilon$ resulted in the solvability condition (2.24), which corresponds to the dispersion relation of the equatorial waveforms. In this section, we present the asymptotic analysis of the non-dimensional dispersion equation (2.24). In particular, we show that the solutions of the dispersion equation of the harmonic equatorial waves derived in Section 2.3 provide a good agreement with the asymptotic solutions of (2.24). The method presented in this section differs from the analysis in Section 2.6.

To gain some insights into the non-dimensional dispersion relation (2.24) provided in Section 2.5, we examine approximations of the solutions to derive analytical estimates for the eigenvalues. To advance with the asymptotic analysis, we use the following relations [see (**48**)]

$$U(\mathfrak{b},z) = \frac{e^{-\frac{z^2}{4}}\Gamma\left(\frac{1}{4}-\frac{\mathfrak{b}}{2}\right)\cos\left(\pi\left(\frac{1}{4}+\frac{\mathfrak{b}}{2}\right)\right)}{2^{\frac{\mathfrak{b}}{2}+\frac{1}{4}}\sqrt{\pi}}M\left(\frac{\mathfrak{b}}{2}+\frac{1}{4},\frac{1}{2},\frac{z^2}{2}\right) - \frac{e^{-\frac{z^2}{4}}\Gamma\left(\frac{3}{4}-\frac{\mathfrak{b}}{2}\right)\sin\left(\pi\left(\frac{1}{4}+\frac{\mathfrak{b}}{2}\right)\right)}{2^{\frac{\mathfrak{b}}{2}-\frac{1}{4}}\sqrt{\pi}}zM\left(\frac{\mathfrak{b}}{2}+\frac{3}{4},\frac{3}{2},\frac{z^2}{2}\right), \tag{C.1}$$

$$V(\mathfrak{b},z) = \frac{1}{\Gamma\left(\frac{1}{2}-\mathfrak{b}\right)}\left\{\frac{e^{-\frac{z^2}{4}}\Gamma\left(\frac{1}{4}-\frac{\mathfrak{b}}{2}\right)\sin\left(\pi\left(\frac{1}{4}+\frac{\mathfrak{b}}{2}\right)\right)}{2^{\frac{\mathfrak{b}}{2}+\frac{1}{4}}\sqrt{\pi}}M\left(\frac{\mathfrak{b}}{2}+\frac{1}{4},\frac{1}{2},\frac{z^2}{2}\right) + \frac{e^{-\frac{z^2}{4}}\Gamma\left(\frac{3}{4}-\frac{\mathfrak{b}}{2}\right)\cos\left(\pi\left(\frac{1}{4}+\frac{\mathfrak{b}}{2}\right)\right)}{2^{\frac{\mathfrak{b}}{2}-\frac{1}{4}}\sqrt{\pi}}zM\left(\frac{\mathfrak{b}}{2}+\frac{3}{4},\frac{3}{2},\frac{z^2}{2}\right)\right\}, \tag{C.2}$$

where the variable z and parameter $\mathfrak{b}$ can take complex values. In the above representations, $U(\mathfrak{b},z)$ and $V(\mathfrak{b},z)$ are the parabolic cylinder functions (see Section 2.5), $\Gamma(\varkappa)$ denotes the gamma function and $M(x,y,\varkappa)$ is Kummer's function of the first kind [see, for example (**48**, **95**, **96**)].

Applying the above relations to the (2.24), yields the following simplified dispersion equation

$$\frac{4\epsilon\Phi^{1/4}e^{-\epsilon^2\sqrt{\Phi}}M\left(-\frac{\Lambda}{4\sqrt{\Phi}}+\frac{1}{4},\frac{1}{2},\epsilon^2\sqrt{\Phi}\right)M\left(-\frac{\Lambda}{4\sqrt{\Phi}}+\frac{3}{4},\frac{3}{2},\epsilon^2\sqrt{\Phi}\right)}{\sqrt{\pi}}=0. \tag{C.3}$$

By taking into account (2.12), (C.3) can be solved numerically to obtain the non-dimensional eigenvalues for the meridional modes. To derive the eigenvalues, we consider asymptotic approximations to the zeros of the Kummer functions in (C.3) for large $\Lambda/\sqrt{\Phi}$.

C.1. Approximations to the zeros of $M\left(-\frac{\Lambda}{4\sqrt{\Phi}}+\frac{1}{4},\frac{1}{2},\epsilon^2\sqrt{\Phi}\right)$ *for large* $\frac{\Lambda}{\sqrt{\Phi}}$

In the following analysis, we consider the asymptotic properties of Kummer's function valid for large $\Lambda/\sqrt{\Phi}$, where the non-dimensional quantities Λ and Φ are defined in (2.12). It is also noted that Λ and Φ are chosen such that the conditions in (2.22) are satisfied. An asymptotic result for the zeros of $M\left(-\frac{\Lambda}{4\sqrt{\Phi}}+\frac{1}{4},\frac{1}{2},\epsilon^2\sqrt{\Phi}\right)$ with large $\Lambda/\sqrt{\Phi}$ is given by the formula [see (**96**)]

$$\sqrt{\Phi}\epsilon^2=\frac{j^2_{-\frac{1}{2},r}\sqrt{\Phi}}{\Lambda}\left(1+\frac{(2j^2_{-\frac{1}{2},r}-3)\Phi}{6\Lambda^2}\right)+O\left(\left(\frac{\sqrt{\Phi}}{\Lambda}\right)^4\right),\quad r=1,2,3,\ldots, \tag{C.4}$$

where $j_{-\frac{1}{2},r}$ is the r-th positive zero of the Bessel function $J_{-\frac{1}{2}}(z)$ of the first kind [see, for example (**48**)]. Noting that (**97**)

$$J_{-\frac{1}{2}}(z)=\sqrt{\frac{2}{\pi z}}\cos(z), \tag{C.5}$$

we obtain the following representation for $j_{-\frac{1}{2},r}$:

$$j_{-\frac{1}{2},r}=\frac{(2r-1)\pi}{2},\quad r=1,2,3,\ldots. \tag{C.6}$$

Applying the above asymptotic relation for the Kummer function, we derive the following approximation for the solutions of (C.3):

$$\Lambda=\frac{(2r-1)^2\pi^2}{4\epsilon^2}+\frac{\epsilon^2}{3}\Phi-\frac{2\epsilon^2}{(2r-1)^2\pi^2}\Phi,\quad r=1,2,3,\ldots. \tag{C.7}$$

The dispersion relation (C.7) corresponds to the approximate odd modes of the dispersion equation (2.46) for the equatorial waves in a narrow band. Taking into account (2.12), the dispersion curves described by the approximation (C.7) correspond to the odd modes shown in Fig. 7 for $n=1$ and $n=3$ (that is for $r=1$ and $r=2$, respectively). In particular, for each value of r, there are three types of curves associated with the equatorial waveforms: westward-propagating inertia-gravity waves, eastward-propagating inertia-gravity waves and Rossby waves. The properties of these waves are discussed in the main text.

C.2. *Approximations to the zeros of* $M\left(-\frac{\Lambda}{4\sqrt{\Phi}}+\frac{3}{4},\frac{3}{2},\epsilon^2\sqrt{\Phi}\right)$ *for large* $\frac{\Lambda}{\sqrt{\Phi}}$

In this section we consider the following asymptotic approximation to the zeros of $M\left(-\frac{\Lambda}{4\sqrt{\Phi}}+\frac{3}{4},\frac{3}{2},\epsilon^2\sqrt{\Phi}\right)$ with large $\Lambda/\sqrt{\Phi}$:

$$\sqrt{\Phi}\epsilon^2=\frac{j_{\frac{1}{2},p}^2\sqrt{\Phi}}{\Lambda}\left(1+\frac{(2j_{\frac{1}{2},p}^2-3)\Phi}{6\Lambda^2}\right)+O\left(\left(\frac{\sqrt{\Phi}}{\Lambda}\right)^4\right),\quad p=1,2,3,\ldots, \tag{C.8}$$

where $j_{\frac{1}{2},p}$ is the p-th positive zero of the Bessel function $J_{\frac{1}{2}}(z)$, which is given by

$$J_{\frac{1}{2}}(z)=\sqrt{\frac{2}{\pi z}}\sin(z).$$

By following a similar approach to the previous section, we obtain the following asymptotic result of $M\left(-\frac{\Lambda}{4\sqrt{\Phi}}+\frac{3}{4},\frac{3}{2},\epsilon^2\sqrt{\Phi}\right)$ for large $\Lambda/\sqrt{\Phi}$:

$$\Lambda=\frac{p^2\pi^2}{\epsilon^2}+\frac{\epsilon^2}{3}\Phi-\frac{\epsilon^2}{2p^2\pi^2}\Phi,\quad p=1,2,3,\ldots. \tag{C.9}$$

Using (2.12), it follows that (C.9) yields an approximate dispersion relation for the waveforms in an equatorial band. Equation (C.9) also provides an approximation to the solutions of (C.3), and corresponds to the even modes of the dispersion relation (2.46). The associated dispersion curves are shown in Fig. 7 for $n=2$ and $n=4$ (that is for $p=1$ and $p=2$, respectively). These curves are related to the inertia-gravity waves and the Rossby waves, and are located inside the shaded region determined by (2.22).

By considering (2.12) together with (C.7) and (C.9), we obtain an approximation for the frequencies and wavenumbers of the equatorial waveforms. From this approximation, the eigenfunctions of the meridional velocity mode can be obtained by using (2.23). The above asymptotic analysis further validates the approximation of the harmonic waves detailed in Section 2.3.